Quantitative magnetic resonance angiography for flow quantification of carotid and intracranial stenosis

Inaugural-Dissertation
zur Erlangung des Doktorgrades
der Medizin

der Medizinischen Fakultät
der Eberhard Karls Universität
zu Tübingen

vorgelegt von

Sobieh, Ahmed Mohammed Abdelaal Mohammed

2016

	Dekan	Professor. Dr. I. B. Autenrieth
1-	Berichterstatter	Professor. Dr. U. Klose
2-	Berichterstatter	Professor. Dr. T. Ethofer

To my home country, Egypt

To my beloved family and fiancée.

Acknowledgment

My earnest gratitude and great appreciation goes to Prof. Dr. Uwe Klose, Department of Diagnostic and Interventional Neuroradiology, Tübingen University and supervisor of this work for his continuous encouragement, suggestions, inspirational ideas, valuable advices, guidance, patience, support and his continuous assistance.

My deep thanks and gratitude goes to Dr. med Till-Karsten. Hauser, Senior Physician at the Department of Diagnostic and Interventional Neuroradiology, Tübingen University Hospital for continuous support, valuable advices and appreciated help.

Special thanks go to Dr. Paul Schoenhagen, Associate Professor, Radiology department Lerner College of Medicine, Cleveland, Ohio for his valuable assistance in final language correction of the doctoral thesis.

My thanks go to Dr. Yosra Helmy, research associate at Ohio Agricultural Research and Development Center, Ohio State University for her continuous support, effort and time.

Ahmed Sobieh

Contents

List of figures

List of tables

List of Abbreviations

CE-MRA	Contrast enhanced magnetic resonance angiography
CTA	Computerized tomography angiography
DSA	Dynamic subtraction angiography
ECST	European Carotid Surgery Trial
HR-MRI	High Resolution MRI
ICA	Internal Carotid artery
MCA	Middle cerebral artery
NASCET	North American Symptomatic Carotid Endarterectomy Trial

PC MRA	Phase contrast angiography
QMRA	Quantitative magnetic resonance angiography
TCCD	Transcranial colour-coded Doppler
TCD	Transcranial Doppler
TOF MRA	Time of flight magnetic resonance angiography
ROI	Region of interest
VA	Vertebral artery
Venc	Velocity encoding

1-Introduction

Cerebrovascular stroke is a major cause of morbidity and mortality in Europe, North America and Asia (1). While the etiology is complex, plaque accumulation and associated narrowing of the extra- and intra-cranial vessels is the underlying pathologic substrate in the majority of ischemic strokes. Specifically, atherosclerotic internal carotid artery stenosis is responsible for a considerable proportion of ischemic strokes (estimates range from 20% to 40%) and transient ischemic attacks (2). Surgical or endovascular revascularization of critical internal carotid artery stenosis is associated with improved outcome; however, it requires the definition of reproducible criteria justifying intervention, based on the quantitative degree of stenosis. In current clinical practice, stenosis severity determined with conventional invasive angiography, is the basis for subsequent clinical management (3). Specifically, clinical guidelines define angiographic stenosis thresholds justifying revascularization. In North American Symptomatic Carotid Endarterectomy Trial (NASCET) and European Carotid Surgery Trial (ECST), angiography was studied in reporting treating carotid artery stenosis of different degrees. Both trials applied different methods for calculation of stenosis severity. NASCET trial demonstrated mild significant benefit in patients suffering from 50 to 69% stenosis and maximum benefit in patients suffering from more than 70% stenosis. The ECST demonstrated a small significant benefit in patients with 70 to 79% stenosis and maximum profit in patients with more than 80% stenosis (4).

Different imaging techniques are used for diagnosis of stenosis, each one has its own advantages and limitations. Digital subtraction angiography is a safe but invasive procedure with a small risk of complications (5). Further, as a planar imaging modality, it also does not allow 3-dimensional reconstruction of vessel anatomy. Advances of non-invasive, tomographic imaging modalities including CTA and MRI/MRA allow detailed visualization of vessel anatomy including 3-dimensional reconstruction and assessment of stenosis severity (6). MRI is particular attractive because of the lack of radiation exposure and the feasibility of angiographic imaging without contrast administration. Specifically, ‘time-of flight’ (TOF) MRA has been shown to be highly accurate in detecting high-grade ICA stenoses, with sensitivity and specificity similar to contrast-enhanced (CE) MRA (sensitivity 91.2% vs. 94.6%; specificity of 88.3%

vs91.9% (2). However, other studies reported that TOF-MRA has a tendency to overestimates the degree of stenosis (7).

Further MRI allows flow visualization and quantification. Prior studies in phantoms and in-vivo found good agreement between flow rates measured by gradient echo sequence and Doppler (8). MRA Flow velocities can be used to calculate the degree of a possible stenosis (9). Combination of different MRI acquisitions allow simultaneous anatomic visualization and blood flow measurements within cerebral arteries (10).

Non-invasive evaluation of vascular anatomy with MRI has a potential role in the initial diagnosis of carotid stenosis prior to revascularization but also during follow-up after the procedure. In-stent restenosis 'ISR' of intracranial stents occurs in up to 25-35% of patients (4, 10-12). Definitive detection of ISR depends on conventional invasive angiography, because of its high spatial resolution and superior visualization of the stented lumen. The non-invasive imaging modalities including CTA, ultrasound, and MRI are limited due to artifacts caused by the metallic stent material furthermore; stents are radio-opaque which hampers diagnosis if in stent restenosis occurred. (13, 14). With MRI imaging, metal related signal void and artifacts limit lumen visualization and may mimic luminal narrowing (15). A potential solution is measuring blood flow within the stented vessel to detect ISR depending on its physiologic, hemodynamic significance rather than its anatomic appearance.

The aim of this project was to develop a new technique for the follow-up examination of patients who were treated by balloon angioplasty and stenting for symptomatic stenosis of the internal carotid artery or major intracranial arteries. Our goals are to implement and optimize sequences for quantitative MR angiography, allowing spatial and time-resolved flow encoding, estimation of the flow velocity, and better characterization of stenosis and assessment of its degrees. Among our objectives was to find a relation between flows in both sides in healthy subjects, to allow us setting a baseline above which we might expect stenosis obscuring flow.

2-Literature Review

Chapter One: Anatomical Overview

In this chapter, an overview of the anatomy of the internal carotid artery, middle cerebral artery, and vertebral artery will be discussed.

2.1.1: Internal carotid artery

There are two internal carotid arteries on each side of the neck arising from the ipsilateral common carotid artery. The right common carotid artery originates from the brachiocephalic artery; the left common carotid artery originates from the arch of the aorta. From its origin to its bifurcation, it runs close to the internal jugular vein and vagus nerve under the anterior border of the sternocleidomastoid muscle. It divides into external and internal carotid arteries at the upper border of the thyroid cartilage. The external carotid artery gives branches to supply the neck, face, and scalp structures. It runs in the neck first medially and then posteriorly and laterally to the internal carotid artery until it enters the parotid gland, where it divides into superficial temporal and maxillary arteries. The anatomy of the internal carotid artery is shown in figure 1.

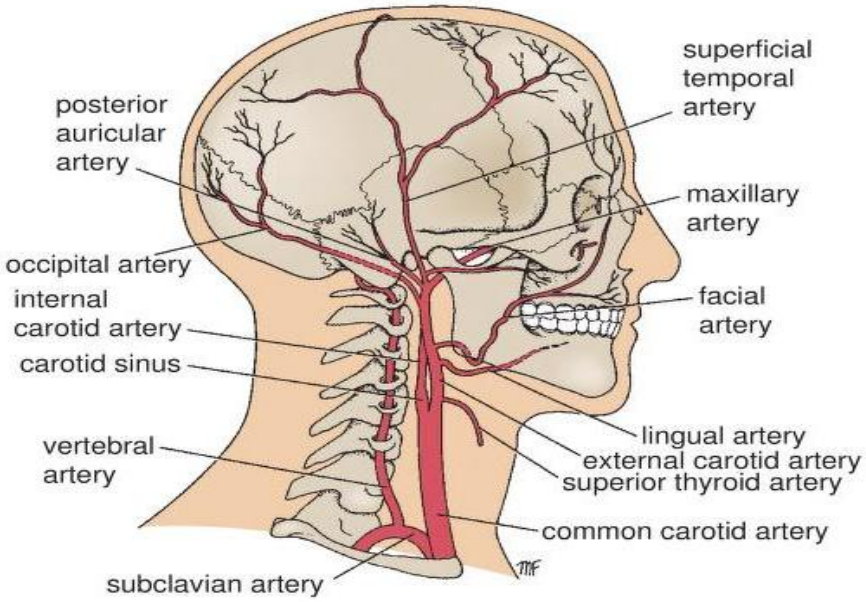

Figure 1: Anatomy of the common carotid artery and its branches (16).

The internal carotid artery provides blood supply to the forehead, part of the nose, eye, and brain. This artery is divided into cervical, petrous, cavernous, and cerebral

segments. The cervical segment starts after its origin from the common carotid artery, where it ascends in the carotid triangle anterior to the transverse process of the upper cervical vertebrae. It lies in the carotid triangle together with the internal jugular vein and the vagus nerve. The sternocleidomastoid muscle covers it anterolaterally. The petrous segment starts as it passes through the carotid canal in the petrous portion of the temporal bone to enter the cranium. The cavernous segment begins as the artery passes in the carotid groove through the cavernous sinus alongside the sphenoid bone body. It terminates in the anterior perforated substance by dividing into the anterior and middle cerebral arteries. Additionally, it gives rise to the ophthalmic artery, posterior communicating artery, and anterior choroidal artery.

2.1.2 Vertebral artery

The two vertebral arteries originate from the first segment of the subclavian artery. They ascend through the foramina of the transverse processes of the upper 6 cervical vertebrae to enter the cranium through the foramen magnum. They unite at the inferior border of the Pons to give rise to the basilar artery. The basilar artery ascends across a groove along the anterior pontine surface. The basilar artery supplies blood to the inner ear, rhombencephalon, and cerebellum. The artery ends by dividing into 2 posterior cerebral arteries on each side.

2.1.3: Middle cerebral artery

This artery originates as one of the two terminal branches of the internal carotid artery. It is located in the lateral cerebral sulcus and supplies the whole lateral cerebral surface except for a strip along the superolateral margin, occipital pole, and inferolateral cerebral surface, which is supplied by the anterior cerebral artery; the posterior cerebral artery supplies the remaining cerebral sections. The middle cerebral artery provides blood supply to cerebral motor areas as well as the internal capsule. It is divided into four segments: the sphenoidal segment (M1) travels from its origin from the internal carotid artery to its bi/trifurcation. The insular segment (M2) crosses the Sylvian fissure. The operator segment (M3) emerges from the fissure, and the cortical segment (M4) is the last segment of the artery (16).

Chapter Two: Intracranial Stenosis

2.2.1: Burden of disease

Stroke is the second leading cause of death globally following coronary heart disease (17). Almost one million patients suffer a first ischemic stroke in the European Union every year (18) . In Germany, a rise in the incidence rate of ischemic stroke ranging from 1.5-1.9 million cases from 2006 to 2025 is expected. This represents a major financial burden for health care. For example it will add more than 51 billion Euros to healthcare costs in Germany (19), represents 3-4% of healthcare expenses in the Netherlands (20). The estimated annually cost in the USA is 57 billion$(1).

2.2.2: Epidemiology

Intracranial stenosis affects mainly the MCA specifically its 1st and 2nd segments followed by internal carotid, vertebral and basilar arteries (21). Stenosis affecting the vertebral-basilar circulation results in 20 % of stroke (22). Stenosis prevalence varies with ethnic group, reaching 33-50% in Chinese patients (23) , up to 29 % in African American,11% Hispanics 11 % and 6-10% in Caucasian (24).

Risk factors

There are multiple risk factors for developing intracranial stenosis, some of which are modifiable and others are not.

Race: Prevalence is higher among African American, Hispanics and Asians compared to White populations. Whites suffer from stenosis at origin of ICA while African Americans suffer more from stenosis of main MCA and supra-clinoid segment of ICA (24).

Age: Prevalence rises as age increases especially when diabetes mellitus, hypertension, hyperlipidemia are present (21).

Sex: Stenosis is more prevalent among men compared to women. In younger patients, stenosis affects mainly basilar artery (25).

Genetics: Several genetic factors share in the pathogensis process of stenosis such as angiotensin converting polymorphism, plasma homocysteine levels, glutathione S transferase omega 1 gene polymorphism. They might impair angiogensis or promote vascular smooth muscle proliferation and endothelial injury (26, 27). Other modifiable risk factors include hypertension (28), metabolic syndrome (29) impaired lipid metabolism and Diabetes Melitus share in pathogenesis process. Increased incidence is associated with increased total cholesterol level and low density lipoprotein. Diabetes impairs fibrinolytic activity through which it induces stenosis (30). Patients with intracranial stenosis suffer from diabetes more than those with extracranial stenosis (29).

Pathophysiology

Stenosis usually caused by an atherosclerotic plaque that starts by monocyte migration into the subendothelial space and their conversion into macrophage. Macrophages engulf lipids and transform to foam cells which accumulate and form plaque. Later smooth muscles migrate to intimal layer and produce collagen which augment plaque progression and fibrous cap formation. Plaque narrows the vessel lumen with subsequent hypoperfusion and thromboembolism distal to the narrowed area. ()

2.2.3: Imaging techniques for clinical diagnosis

Neuroimaging techniques have an important role in diagnosis of intracranial atherosclerotic diseases either through vessel visualization or determining their flow characteristics. They can establish diagnosis of acute ischemic stroke, determine eligibility for thrombolytic therapy or for endovascular revascularization, detect large artery occlusion, assess viable ischemic brain tissue, and assess cerebral collateral circulation (31) .

2.2.3.1: Transcranial Doppler

Doppler techniques provide non-invasive, fast dynamic real time evaluation of intracranial vessels and stenosis. It could be performed bedside, many times with no harm to patients. They measure blood flow velocity which detects and grades stenosis

depending on peak systolic velocity, mean systolic flow velocity, velocity ratios of segments before and after stenosis (32). They can evaluate presence of collaterals at Circle of Willis and their sufficiency that has significant impact on prognosis. Definite cut off values have been set for accurate diagnosis of MCA stenosis. In case of 50% and 75 % stenosis, the peak systolic velocity is 140 cm/s and 180 cm/s.

Transcranial color-coded Doppler sonography (TCCD) can differentiate accurately between MCA trunk stenosis and stenosis of the terminal part of the ICA (33). Doppler Techniques can differentiate between intracranial and extracranial sources of emboli (34). In table 1, an explanation of criteria and their quantitative values that aid in diagnosis of internal carotid artery stenosis using Doppler ultrasound is shown. Diagnosis is according to North American symptomatic Carotid Endarterectomy Trial Classification (35). Potential limitations include high operator dependency, potentially limited windows (5) and results might be influenced by differences in location and number of stenosis (32).

Table 1: Diagnostic criteria for the determination of internal carotid artery stenosis using spectral Doppler Ultrasound (35).

Percent stenosis (NASCET)	**Systolic velocity cm/sec**	**Peak systolic velocity ratio ICA $_{PSV}$ / CCA $_{PSV}$**	**St Mary ratio ICA $_{PSV}$ / CCA $_{EDV}$**
<50	<125	<2	8
50-59	>125	2-4	8-10
60-69	>125	2-4	11-13
70-79	>230	>4	14-21
80-89	>230	>4	22-29
>90 but < near occlusion	>400	>5	>30
Near occlusion	High, low string flow	Variable	Variable
Occlusion	No flow	Not applicable	Not applicable

2.2.3.2: Computerized tomography angiography (CTA)

Contrast enhanced CTA is a non-invasive tool allowing precise visualization of lumen and vessel wall. Advantages are high spatial resolution and ability for 3D multiplanar reconstruction, less distortion artifact and a high acquisition speed that provides excellent appreciation of anatomic relationships among vessels, bones and soft tissues. CTA is almost 100% sensitive for detecting intracranial occlusion when compared to DSA (36). When stenosis is more than 50%, the sensitivity reaches 97.1% while specificity is 99.5%. This technique can also detect the vessel patency in posterior circulation. It offers a high inter-reader reliability in quantification of stenosis. It is independent of hemodynamic effects. CTA involves the application of X ray emitted from gantry at different angles obtaining projection images that are analyzed and provide the opportunity for reconstructed images. This allows limitless reformation of potential angiographic planes for any LAO,/RAO angulations (6).

Limitations include radiation exposure , risk of nephrotoxicity due to contrast injection, artifact caused by vessel wall calcification and metal artifact, limiting assessment in patients with advanced, calcified atherosclerotic disease and after vessel stenting (36). CTA is not suitable for arteries smaller than 0.7 mm (37). Window and level settings should be optimally adjusted to precisely visualize vessels to avoid over or underestimation of stenosis. It demands high skill for optimal contrast gradient-timing so as to avoid contamination with adjacent structures (6). .

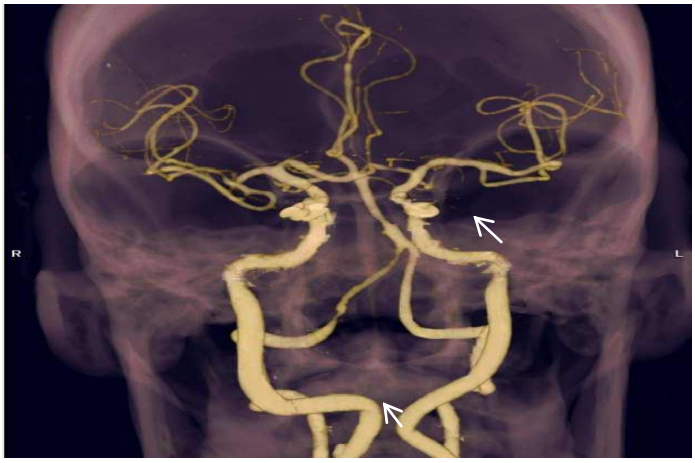

Figure 2 illustrates stenosis of the MCA and VA diagnosed with CTA (5).

2.2.3.3: Digital Subtraction Angiography (DSA)

DSA is the gold standard for evaluating intracranial stenosis and occlusion. It is performed through injecting a radio-opaque dye via an intra-arterial catheter through either the femoral or radial arteries. Two to four images per second are produced using a digital plate panel detector. Visualization of arterial structures is performed by subtracting the pre-contrast images from the post-contrast injection and removing bones and soft tissues. The data can be recalled for viewing on a video screen, and successive images can be created allowing for detection of abnormalities. The serial images show changes in the contrast appearance over time (temporal subtraction) and at varying X-ray intensities (energy subtraction). If no technical complications are encountered, most examinations can be completed in 25 to 45 minutes (38).

DSA has multiple advantages including its ability to provide anatomic localization, excellent visualization of vessel contour in addition to measuring degree and length of stenosis ,as shown in figure 3, and assessment of collateral circulation. 3D reconstructed images can be incorporated from the raw data to provide even greater detail (6) .

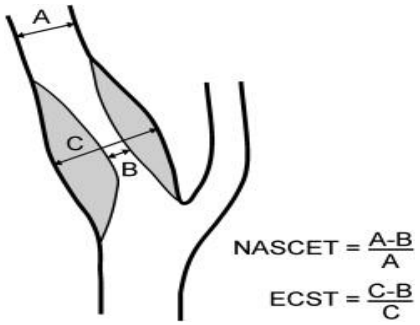

Figure 3: Schematic diagram of a stenosis of the internal carotid artery showing NASCET and ECST methods of stenosis calculation (39).

On the other hand, the major disadvantage is the necessity of highly skilled neurointerventional radiologist to perform the study, nephrotoxicity associated with iodinated contrast. Small risk of serious complications, including stroke, arterial dissections, infection of puncture site, thrombosis of punctured artery resulting in limb ischemia and formation of pseudo aneurysms (5). In figure 4, stenosis affecting the right vertebral artery is detected with DSA.

Figure 4: DSA showing stenosis of the right vertebral artery (arrow) (5).

2.2.3.4: Magnetic Resonance Angiography (MRA)

2.2.3.4.1: Phase contrast (PC) and time of flight (TOF) MRA

Phase contrast MRA techniques utilize the velocity differences which induce phase shift of mobile spins due to velocity differences to acquire image contrast in flowing vessels. They influence magnetization phase of spin where the phase of immobile spins is zero, while for mobile spins, the phase is non zero. Time of flight MRA techniques depend on flow and movement of blood protons through the imaging plane. They influence magnetization magnitude of spins, where the magnitude of mobile spins is large and that of static spins is small, As a consequence contrast between flowing blood and static tissues is derived. Both techniques could develop 2D or 3D acquisitions.

Their advantages include non-invasiveness, absence of radiation exposure and no need for iodinated contrast injection with its subsequent sequel. They require very low user interaction for acquisition and processing of images. TOF-MRA techniques have 70% sensitivity for intracranial stenosis and 81% for occlusion compared to DSA and a negative predictive value of 98% for stenosis and 99% for occlusion (6). Phase contrast MRA techniques can determine flow direction and velocity. Potential limitations include sequences are susceptible to motion artifacts , to changes in the direction of the flow due to its dependence on changes in blood flow, they offers spatial resolution

lower compared to DSA and CTA. At highly stenosed points, dephasing artifact and loss of flow signal intensity take place reducing its the ability to differentiate between high grade stenosis and occlusion (5). Figure 5 shows a posterior cerebral stenosis detected with TOF-MRA.

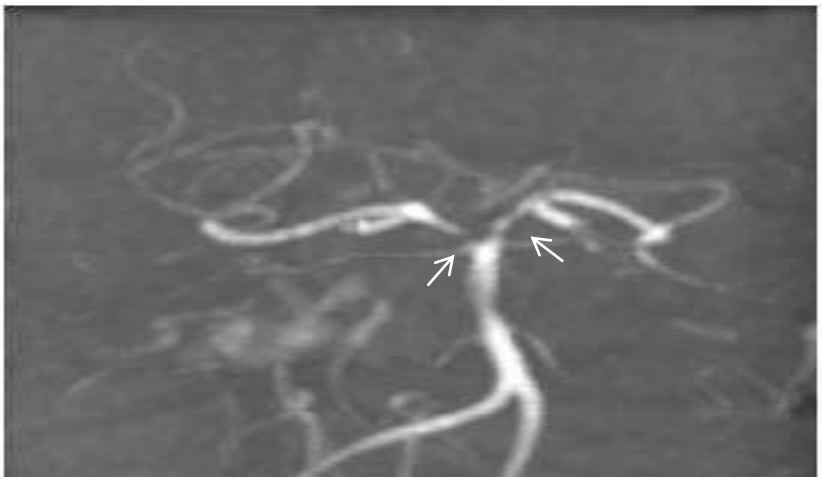

Figure 5: MRA showing stenosis seen in the bilateral posterior cerebral arteries (arrows) (5).

2.2.3.5: Contrast Enhanced (CE) MRA

In this technique gadolinium is injected to selectively shortens T1 of blood with subsequent increase in the magnitude of moving blood while the magnitude of the static tissues and veins remain the same to provide better anatomic delineation of vascular structures and improve assessment of areas of hanging flow direction (40). It is less affected by intravoxel dephasing observed with complex flow. Fewer artifacts are observed. 2D and 3D acquisitions could be acquired.

The most important limitations is gadolinium injection which has multiple side effects ranging from nausea, vomiting, allergic reactions (hives, erythema), nephrogenic systemic fibrosis in patients with severe renal failure and brain deposit with repeated usage. Furthermore expertise is required to time the image acquisition to minimize venous contamination (5) .

2.2.3.6: High resolution MRI (HR-MRI)

This technique offers high axial resolution of 250×250 μm (41) by creating thin slices through the vessel wall. This permits atherosclerotic plaque imaging especially those which still didn't cause stenosis on MRA. This technique can determine plaque size, composition and biological activity(42). This technique is capable of detecting etiologies that cause stenosis other than atherosclerotics etiologies. It can be used in guiding endovascular intervention of basilar artery (43) .

2.2.3.7: Quantitative MRA (QMRA)

QMRA is a technique that is capable of measuring blood flow volume (44). It combines time-of-flight MRA and phase-contrast MRA rendering it a unique technique. It can analyze arterial waveforms providing potentially important physiologic information in patients with various cerebrovascular diseases (45).

QMRA can be used to assess cerebrovascular circulation in healthy individuals and in patients with various cerebrovascular conditions. It is capable of assessment of vascular hemodynamic to stratify risk of stroke in symptomatic vertebrobasilar disease (46), evaluate vertebrobasilar flow in patients with subclavian steal syndrome (47), assess blood flow after extracranial artery Wingspan stent placement (48), evaluate leptomeningeal collateral blood flow in large vessel cerebrovascular disease (49) and to quantify shunt reduction in transarterial embolization of vein of Galen malformations (50).

In QMRA 3D TOF images are acquired with reconstructions in axial, sagittal and coronal planes. A 3D surface-rendering of the vascular anatomy is produced to locate the desired vessel and a slice is positioned perpendicularly to the vessel. Velocity encoding is adjusted automatically and phase images are obtained and forwarded to NOVA software containing both magnitude and phase images creating a flow report (51).

Chapter Three: Fluid Dynamics in Circulatory System.

2.3.1: Vascular hemodynamic

Maintaining adequate blood flow is essential for the functioning of various organs. Blood flow is defined as the blood volume passing through each point of the vessel in a unit of time and is usually expressed in milliliters per minute (mL/min). Pressure is the force that pushes the blood through the vessel and is expressed in millimeters of mercury (mmHg). Pressure varies over the course of the blood vessel. The pressure is produced by the cardiac ventricle and decreases throughout the vessel due to resistance that impedes flow. Resistance occurs due to blood viscosity and the radius of the blood vessel. Factors affecting flow are estimated through Poiseuille's law, which states:

$$F = \frac{\pi \Delta P r^4}{8 L \eta} \qquad (1)$$

where F is flow, ΔP is the difference in pressure, r is the radius of the blood vessel, L is the length of the blood vessel, and η is the blood viscosity.

In a healthy individual, viscosity and the length of the blood vessel are constant; however, in some diseases, viscosity is changed, which affects resistance. Vessel radius exerts the most powerful effect on resistance, so that with small variations in radius, resistance will vary dramatically (as r^4 is inversely proportional to resistance). Radius is therefore the main factor for controlling resistance in the cardiovascular system. Flow is proportional to change in pressure. Flow is also proportional to the 4^{th} power of the internal radius of the tube, indicating the great effect of the radius on flow. This is applicable in cases of unrestricted flow; in arteries, the situation is different as arteries are not open tubes (52).

2.3.1.1: Laminar flow:

Blood flow in the straight vessels under steady flow situations is laminar. Laminar flow occurs when blood moves in layers parallel to the vessel wall. Particles move in a very orderly manner. The highest velocity is found in the center of the vessel, and the lowest velocity is found along the vessel wall. The direction of the flow is parallel to the vessel wall. Normal laminar blood flow may become turbulent when the rate or velocity of

blood flow increases, when it passes by an obstruction in a vessel, when it makes a sharp turn, or when it passes over a rough surface. Turbulence is related to the diameter of the vessel and blood viscosity.

The Reynolds number ***(Re)*** is the most important dimensionless number describing fluid flow. As it increases, the probability of turbulence increases:

$$Re = \frac{\rho v D}{\eta} \quad (2)$$

where ρ is the fluid density, v is the mean fluid velocity, D is the diameter, and η is the fluid viscosity. The critical Reynolds number is 2200. Viscous effects are dominant with low Reynolds numbers (<2200) and flow is laminar; with high Reynolds numbers (>2200), the flow is turbulent (53).

The Womersley number ***(α)*** is another important dimensionless number used for pulsatile flow to express the ratio of oscillatory inertia force to shear force. It is estimated as follows:

$$\alpha = L\left(\frac{\omega \rho}{\square}\right)^{1/2} \quad (3)$$

where L is the radius of the vessel, ω is the angular frequency of the oscillations, ρ is the kinematic viscosity, and μ is the dynamic viscosity of the fluid.

Both the Reynolds and Womersley numbers govern dynamic similarity (54).

2.3.1.2: Turbulent Flow:

In cases of turbulent flow, the direction of the flow is no longer parallel to the vessel wall and blood flows in different directions. Turbulent flow displays rapid variations of pressure and flow velocity in time and space. It has crosscurrents and eddies, and the fastest velocities are not necessarily in the middle of the stream. In accelerating flow, turbulence is delayed, whereas it occurs faster in decelerating flows (55). Turbulent flow occurs distal to a stenosis because fluid accelerates in the narrow segment of the stenosis and decelerates in the distal expanding segment. In severe stenosis, turbulence can begin with Reynolds numbers as low as 50 (55). This turbulence widens the vessel

after the stenotic segment. The flow pattern for both types of flow is shown in figure 6; the first image represents laminar flow, in which streamlines flow parallel to the vessel wall in an organized arrangement, and the second image represents turbulent flow, in which streamlines run randomly in a chaotic pattern.

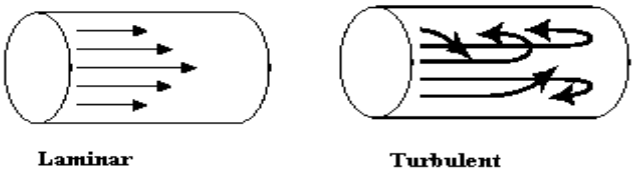

Figure 6: Types of flow (52).

2.3.1.3: Bernoulli's principle

The basis of Bernoulli's principle is conversion of energy, where kinetic energy and pressure energy are interconverted. The principle states that in steady flow, the sum of all forms of energy of a fluid along a streamline is the same at all points, so the sum of kinetic energy, potential energy, and pressure energy remains constant. When fluid passes through a stenosis, kinetic energy increases, velocity increases, and pressure decreases (53). Figure 7 illustrates this principle: the cross-sectional area is reduced in the middle of the tube with subsequent velocity increase. In the distal part of the tube, velocity decreases as area increases.

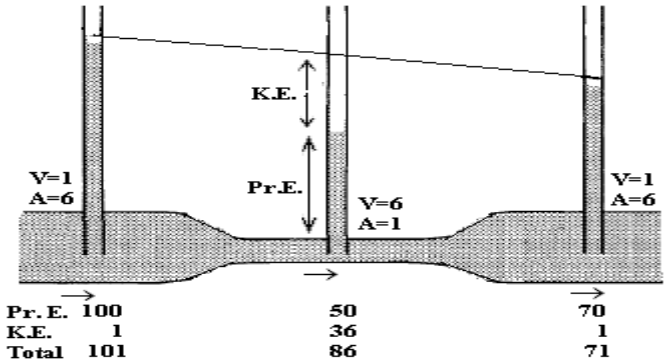

Figure 7: Diagram showing Bernoulli's principle. (A) stands for cross-sectional area, (V) stands for velocity, Pr.E. stands for pressure energy, and K.E. stands for kinetic energy (56).

2.3.2 Flow in stenosis

According to Bernoulli's law, acceleration of the flow decreases the local pressure at the neck of a high-grade stenosis, and in highly advanced situations, the external pressure may be higher, leading to collapse of the artery at the neck due to insufficient pressure to maintain the lumen patency. Consequently, there is a critical degree of stenosis for a given flow rate above which the pressure cannot overcome the energy loss at the neck and the stenosis will collapse, resulting in choking of the flow. Downing and Ku found that in a one-dimensional model with 80% degree of stenosis, there was a >100-mmHg decrease in local pressure, and the flow was choked at a velocity of 0.3 m/s (57). These values are in the physiological range, and this scenario is very likely to occur in vivo, although the collateral circulation might affect the outcome. A larger pressure decrease because of stiffer stenosis will result in collapse of the vessel (58). Rosenfeld and Einav demonstrated that as the stenosis becomes more serious, the strength and total number of vortices increase, creating a train of vortices whose front propagates at a much higher speed because of vorticity multiplication (59). Pressure decrease across the stenosis is affected minimally by the eccentricity of the stenosis; however, it is dominantly affected by the length of the stenosis (60). In figure 8, the effects of 50% and 75% vessel stenosis on streamlines and velocity vectors are illustrated.

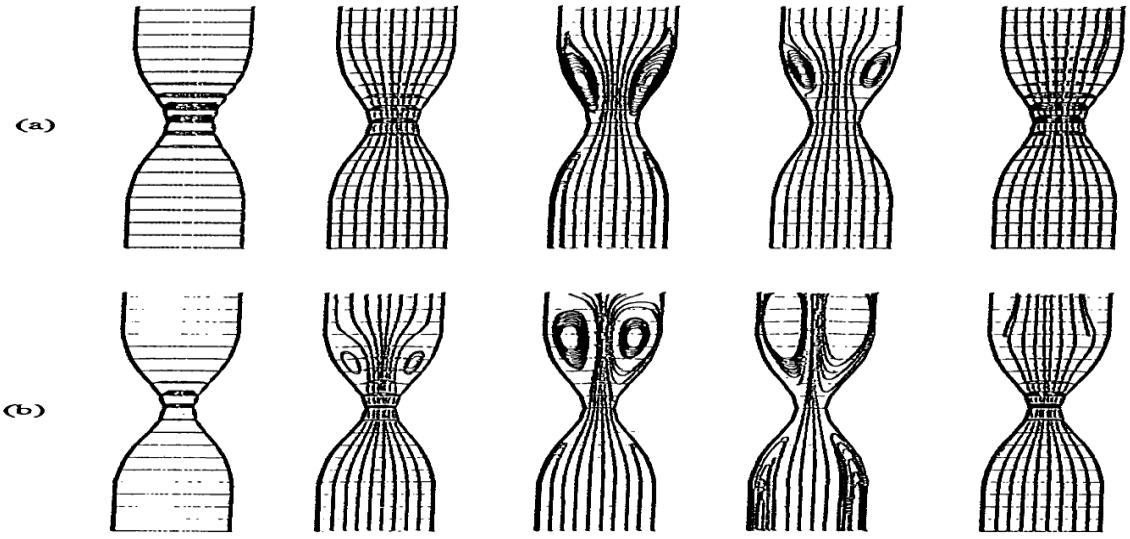

Figure 8: Symmetry plane of a 3D vessel showing streamlines and velocity vectors for axisymmetric decrease in vessel radius by (a) 50% and (b) 75% (61).

As the degree of stenosis increases, turbulence is likely to occur downstream of the stenosis, even in cases with moderate Reynolds numbers. For pulsatile flow, velocity fluctuations decrease as the flow accelerates and increase during deceleration. The turbulent intensity is also greater in a narrower stenosis (62).

Johnston and Kilpatrick demonstrated that with a mild smooth stenosis, there is a lower pressure decrease, whereas for a serious smooth stenosis, the pressure decrease is actually higher than for its irregular counterpart. Blood hemodynamics through a stenosis are affected by geometric and physiological features such as curvature, extent, and stenosis asymmetry, as well as the shape of the pulsatile waveform (63).

2.3.4: Factors affecting blood flow

Cardiac output, the amount of blood pumped to the aorta by the heart each minute, equals 5 L/min. As the pressure difference increases, flow increases; as resistance increases, flow decreases. Regulation of blood flow through a blood vessel is determined by blood pressure and resistance. Resistance depends on blood vessel length, viscosity, and lumen size (64).

Chapter Four: Magnetic Resonance Imaging

2.4.1: Overview of MRI

Hydrogen atoms are the most abundant atoms in the human body. The nucleus of a hydrogen atom has a magnetic field around it, which is randomly oriented in the absence of a magnetic field. In the presence of a magnetic field, the net magnetization vector is the net magnetic moment of hydrogen ions reflecting the relative balance between spin-up and spin-down nuclei. Each hydrogen nucleus is spinning on its axis. When an external excitation pulse is applied, magnetization occurs in the transverse plane, producing an MR signal in a receiver coil. Two exponential processes occur in the tissue: T1 recovery, in which longitudinal magnetization recovers, giving energy to the surrounding lattice (spin lattice relaxation); and T2 decay, in which magnetic fields of neighboring nuclei interact with each other, leading to decay of transverse magnetization (spin-spin relaxation).

MRI sequences consist of radiofrequency excitation pulses and gradients for spatial encoding (2D or 3D). The user must choose the sequence parameters (TR, TE, matrix, flip angle, field of view) that will produce the best compromise among contrast, speed, and spatial resolution. There are 2 main sequence families: spin echo sequences and gradient echo sequences, which differ based on the type of echo recorded.

In this chapter, an overview of gradient echo pulse sequence, frequency encoding, phase encoding, 3D spatial encoding, signal to noise ratio, spatial resolution, MRA, and cardiac triggering will be provided.

2.4.2: Gradient echo pulse sequence

The gradient echo pulse sequence uses variable radiofrequency excitation pulses, flipping the magnetization vector through variable flip angles less than 90° and converting part of the longitudinal magnetization in the transverse plane, which induces a signal in the receiver coil. A bipolar readout gradient is needed for echo creation, as no 180° refocusing pulse is applied. The design of this sequence is shown in figure 9. A

dephasing gradient is applied before the frequency-encoding gradient, resulting in an echo. The readout gradient has a dephasing stage and a rephrasing stage. The dephasing stage is in reverse sign of the readout gradient and matches half of the reading gradient dephasing effect. In the first half of the readout, the readout gradient rephases the spins; dephasing of spins takes place in the second half because of the readout gradient dephasing effect. Echo time is the time between the application of the radiofrequency pulse and the signal peak induced in the coil. The flip angle sets the magnetization portion in the transverse plane (that produces the NMR signal) and the quantity of magnetization on the longitudinal axis. A flip angle less than 90° is applied, decreasing the amount of magnetization into the transverse plane; therefore, longitudinal magnetization recovers more rapidly, allowing for lower TR/TE and minimizing scan time. Short TR offers new contrasts between tissues and a stronger MR signal. However, there is a lack of compensation for magnetic field inhomogeneities with this technique. Gradient echo pulse sequences also contain susceptibility artifact.

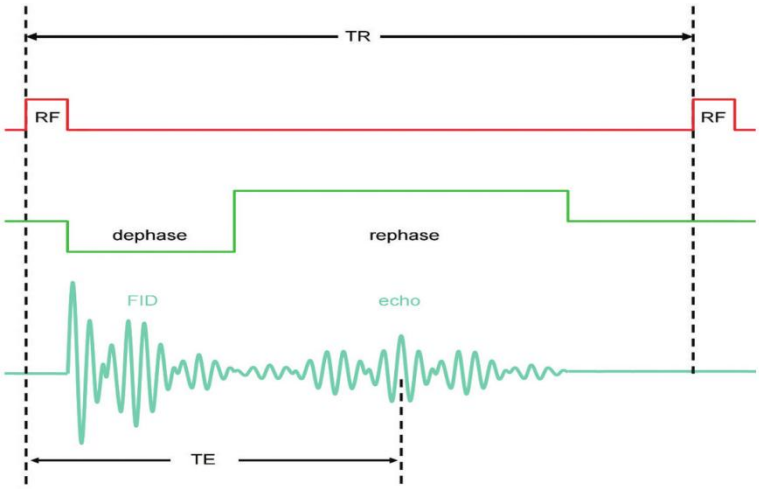

Figure 9: Gradient echo sequence (65).

2.4.3: Frequency encoding

Frequency encoding involves assigning the signal coming from the slice along the long axis of the anatomy. A linear change of the precessional frequency of the signal along the axis of the frequency encoding gradient occurs when it is turned on and subsequent frequency dependent signal location along the axis of the gradient takes place. Each

signal sample corresponds to a given piling-up of the gradient effect on the whole splice signal: the longer the time, the more the spins are affected by the gradient and the greater their phase modification. The gradient is turned on during the rephasing and dephasing portions of the echo and the peak. The frequency field of view is the size of the anatomy covered during the scan and is defined by the steepness of the slope of the frequency encoding gradient. All signals from the same slice are kept in k-space and then processed to form an image of the slice plane.

2.4.4: Phase encoding

This process involves assigning the signal coming from the slice along the short axis of the anatomy either in the horizontal or vertical direction. When the gradient is turned on, protons precess in different phases. The slope steepness of the phase encoding gradient defines the degree of phase shift between two points along the gradient. In the absence of phase encoding, the signal will originate from the whole slice; for this reason, multiple phase encoding steps are required to obtain enough data to reconstruct the image. To perform the various phase encoding steps, the gradient is applied with various regularly incremented values.

2.4.5: 3D Spatial encoding

In 3D acquisitions, an entire volume or a thick slice is excited at every repetition, and phase encoding is added in the 3rd dimension with respect to the phase and frequency encodings. This increases the acquisition time, spatial resolution, and signal to noise ratio and permits fine section and multiplanar reconstructions.

The duration of a 3D imaging sequence is defined as

$$\text{Duration} = TR \cdot NPy \cdot NPz \cdot Nex$$

where TR is the repetition time, NPy is the number of encoding steps in the y-axis, NPz is the number of encoding steps in the z-axis, and Nex is the number of excitations.

2.4.6: Signal to noise ratio (SNR)

SNR is the ratio of the amplitude of the signal obtained to the average amplitude of the background noise. Precession of the net magnetic vector in the transverse plane creates signal in the receiver coil. Frequencies present randomly in space and time, which

creates noise, distorting the signal from transverse magnetization of spins and degrading image information. The factors affecting SNR include:

1. **Magnetic field strength of the system:** As the field strength increases, more magnetization is available for spins, increasing SNR.
2. **Proton density of examined area**: This determines the amplitude of the signal received: the higher the density, the higher the signal received.
3. **TE, TR, and flip angle**: These factors control the degree of magnetization and hence the amplitude of the signal. A long TR increases SNR, whereas a long TE decreases SNR. The lower the flip angle, the lower the SNR.
4. **Voxel volume:** This is the volume of tissue within the patient. Large voxels contain more spins, producing a higher signal. Voxel is determined by the pixel area and slice thickness, where pixel area = FOV dimension / matrix size.
5. **Receive bandwidth**: The receive bandwidth represents the range of frequencies sampled during application of the readout gradient. A decrease in receive bandwidth leads to less sampled noise compared to signal, decreasing the readout gradient intensity and causing slower sampling of the signal. Background noise has a fixed intensity at all frequencies.
6. **Number of excitations** (NEX): NEX is the number of times in which data are gathered with the same phase encoding slope amplitude. It defines the amount of data stored in each K-space line. Doubling the NEX doubles the data containing both noise and signal. Noise is random, but signal is not; doubling NEX increases the SNR by $\sqrt{2}$.
7. **Coil type:** The coil type affects the amount of received signal and SNR. Coil position is also important; the volume of the imaged tissue must fill the sensitive volume of the coil optimally to improve the signal received.

2.4.7: Spatial resolution

Spatial resolution refers to the ability to clearly distinguish between two separate points. It is controlled by voxel size; small voxels result in good spatial resolution and vice versa. Spatial resolution increases with increases in the matrix but decreases with

increasing FOV and slice thickness. Square pixels offer better resolution than rectangular ones, as the image is equally resolved along the frequency and phase axis.

2.4.8: Magnetic resonance angiography (MRA)

There are special MRI techniques that maximize vascular contrast by enhancing signal from flowing blood or suppressing signal from stationary tissues.

MRA techniques include:

1. Time-of-flight MR angiography (TOF-MRA)
2. Phase-contrast MR angiography (PC-MRA)

2.4.8.1: Time of flight MRA (TOF-MRA)

With this technique, signal depends on flow-related enhancement providing information about flowing blood perpendicular to the slice plane. It applies an incoherent gradient echo pulse sequence and gradient moment rephrasing to saturate stationary spins and fully magnetize inflow spins, producing a high vascular signal with proper flip angles and TR values. TOF-MRA can be acquired with 2D or 3D acquisitions. 3D acquisitions are optimal for obtaining high-resolution images and for evaluating smaller vessels with high-velocity blood flow (intracranial vessels). 2D TOF-MRA acquisitions can evaluate slow flow, providing a wider area of coverage.

A saturation pulse is placed outside of the imaging volume in the direction of flow to be suppressed to avoid potential pitfalls. TOF-MRA is sensitive to flow perpendicular to the FOV and slice. Any flow parallel to the FOV can be saturated along with the stationary tissue, especially if the flow velocities are slow relative to the TR. Tissues with short T1 times (such as fat or hemorrhage) will be bright on TOF-MRA images. TE should be kept short to minimize intravoxel dephasing, phase ghosting, and subsequent signal loss. Magnetization transfer contrast and TE are applied to minimize unwanted background signals.

The advantages of TOF-MRA include sensitivity to slow flow, reduced sensitivity to intravoxel dephasing, and reasonable scan time. Its disadvantages include sensitivity to T1 effects; additionally, saturation of in-plane flow and enhancement are limited to flow entering the field of view or very high-velocity flow. 2D-TOF offers a large area of coverage yet has lower resolution than the resolution of 3D inflow studies. 2D-TOF also shows saturation of in-plane flow, and patient motion can cause data misregistration between the individually acquired slices; vessel borders may appear serrated. 3D-TOF offers high resolution for small vessels and is more tolerant of patient motion, demonstrating high SNR where vessels appear less serrated on the reformatted image. However, 3D-TOF also shows saturation of in-plane flow and has a small area of coverage.

2.4.8.2: Phase-contrast MRA

Phase-contrast MRA is a sequence related to in-phase change of flowing blood. This variation relies on blood velocity, flow direction, and the type of scan used. It provides information about vascular anatomy, flow velocity, and flow direction. Blood flow velocity differs based on physiologic status, type and size of vessel, and pathology within the vessel. An oscillator in the scanner electronics is used as a reference to detect phase shift and is also used for position encoding in MRI. Phase has a 360° range, beyond which the same values repeat, causing aliasing.

The phase-contrast sequence is a gradient echo pulse sequence with small flip angles to prevent saturation and with additional gradient pulses that create changes in the nuclear phases of flowing blood spins. Applied bipolar gradient pulses, including pulses with two lobes equal in strength but opposite in charge, allow for differentiation between stationary tissues and spins within flowing blood by manipulating the phase position of spins. The PC sequence has high sensitivity to fluid motion, so it can be used in clinical blood flow analysis. It can also be used to evaluate blood flow with multiple directions and multiple velocities. This technique can create two types of images: magnitude and phase images. In magnitude images, vessels show high signal and a suppressed

background because of short TR, allowing incomplete recovery of magnetization. In phase images, the signal is linearly proportional to the velocity of the blood. The direction of flow appears bright when flow is in the same direction as the velocity encoding gradient, whereas flow in the opposite direction appears black. This technique can therefore be used to localize vessels that can then be more thoroughly evaluated with other techniques. 3D techniques offer an SNR and spatial resolution better than those of 2D techniques and also offer the ability of reformatting. 3D PC-MRA images are acquired for smaller vessels, when multidirectional vascular information (eg, flow velocity and flow direction) is required. 2D PC-MRA techniques provide information about direction and velocity of flow in addition to information about multidirectional flow in a reasonable scan time.

Precise lumen area delineation demands high in-plane resolution, which is necessary to accurately estimate the mean vessel velocity. The signal level of adjacent tissues controls the partial volume effects at vessel edges, and thicker slices will misalign; therefore, thin slices and high spatial resolution are important to overcome these effects. Voxels' dimensions and their alignment with flow are also important, as it may contain a range of velocities (65).

2.4.8.2.1: Velocity encoding

Phase-contrast MRA is sensitive to flow, offering the ability to acquire functional blood quantification and morphological data simultaneously. Flow-dependent phase effects are used to quantify flow by applying appropriate velocity encoding gradients. Two datasets with different velocity-dependent signal phases and with identical acquisition parameters are subtracted to calculate the velocities of moving spins. Bipolar gradients are used for velocity encoding, as these result in no phase encoding of stationary spins; for moving spins, phase change is proportional to gradient amplitude and duration and is linearly dependent on flow velocity. Velocity-dependent phase shifts can be determined by adjusting the first gradient moment (M1) through a change in total bipolar gradient duration and/or gradient strength G. M1 sets the velocity induced signal phase for the fixed velocity approximation so that appropriate control of the first

gradient moment can be utilized to encode spin flow. For filtering background phase effects (φ0) due to field inhomogeneity, two measurements with variable first moments ($M1^{(1)}$) and ($M1^{(2)}$) (inversed gradient polarities) are used to isolate the phase shifts due to velocity and to encode flow along a single direction. Phase images of these two measurements are subtracted, resulting in phase differences (Δφ) that are directly proportional to the encoded velocities (v) and differences in first gradient moments ($\Delta M = M1^{(1)} - M1^{(2)}$) (66). The design of a PC sequence with flow-compensated and flow-encoded gradients is shown in figure 10.

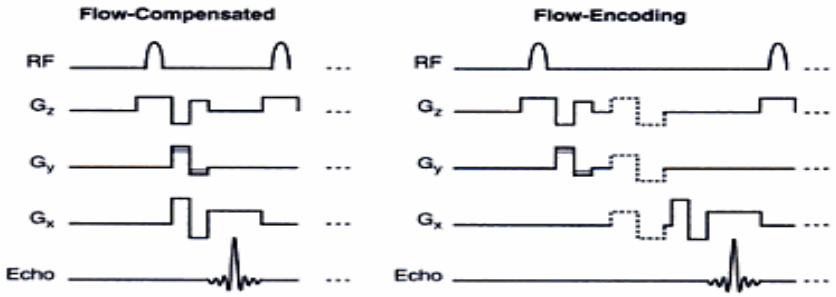

Figure 10: PC sequence using flow compensated and flow encoded gradients (67).

Velocity encoding works only in the phase range of -π to π. The maximum velocity needed for a phase change of π is calculated as $venc = \pi\gamma\Delta M1$; this equation determines the possible velocity sensitivity. Velocity encoding is defined by the difference between the first gradient moments used for velocity encoding. The highest expected velocity should be used to set the velocity encoding (venc-factor) to avoid phase wrapping. Linear flow results in velocity dispersion with subsequent phase dispersion within a voxel, and net signal loss from flowing spins occurs. This velocity-dependent phase dispersion can be corrected with velocity compensation. This is achieved by adding positive and negative areas to the gradient pulses used for slice selection and readout. Flow compensation gradients null phase dispersion effects. In flow compensation, a reference scan is acquired with vanishing zero and first gradient moments, and then a second scan is acquired for velocity encoding with added bipolar gradients and identical parameters. A diagram of a PC pulse sequence with flow-encoded and flow-compensated gradients is shown in figure 10 (68). The reference scan produces background phase images only ($M1^{(1)} = 0$), whereas the second flow-sensitive scan is used to determine velocity sensitivity ($venc = \pi\gamma\Delta M1^{(2)}$). The phase-contrast sequence is

sensitive for the velocity component along the flow-encoding gradient only; therefore, one dedicated flow-encoding gradient for each orthogonal direction of space is required. A PC sequence is composed of four acquisitions: one flow-compensated measurement and three flow-encoded acquisitions in the X, Y, and Z directions. Phase and magnitude images are obtained by subtracting flow-encoded and flow-compensated datasets (68).

2.4.8.2.2: Physical limitations of MRI derived velocity estimation

1-Spatial resolution effects

Short TR values are required to perform temporal acquisitions, consequently limiting the available spatial resolution. Poor spatial resolution leads to partial volume effects in which a pixel will include spins at different velocities, including stationary spins, leading to an average pixel value that underestimates the true peak velocity value (69). Poor spatial resolution decreases the capability to detect small vessels during diastole when the signal is low, inhibiting accurate ROI selection for flow quantification. The change in velocity is masked by additional averaging in the through-plane direction that occurs when slice thickness is larger than the in-plane (x,y) resolution by a factor of >2 (70).

2-Angular dependence

To perform velocity encoding in the through-plane direction, the image plane should be perpendicular to flow direction. When the scan plane deviates from the flow direction by angle β, the velocity (v) will decrease to vcosβ. The slice thickness will also add to errors because of nonorthogonal scan planes ((69),(70)).

3-Velocity encoding limitations

Inappropriate venc values lead to phase unwrapping and signal loss. Venc settings should be set 20% higher than the greatest expected velocity; higher venc settings will have a negative influence on the SNR of the phase image, which will subsequently influence the precision of the maximum velocity values. This has been shown in vitro for steady-state flow; for pulsatile flow, which demands the detection of high systolic peaks and low diastolic velocities, data are lacking (70).

2.4.9: Triggering

2.4.9.1: Cardiac Triggering

Cardiac triggering synchronizes a pulse sequence to the cardiac cycle of the subject. Pulsatile blood flow produces phase mismapping. Cardiac triggering forms images at various cardiac phases with the goal of acquiring an entire set of consistent k-space data at approximately the same portion of the cardiac cycle, free of motion artifacts. It uses the electrical cardiac signal or vascular bed mechanical flow for triggering each pulse sequence; this can be achieved through ECG triggering or peripheral triggering. Figure 11 shows slice acquisition with ECG triggering.

2.4.9.2: Peripheral Triggering

This method depends on the optical properties of the blood. A photosensor is attached to the subject's finger to detect the increase in blood volume in the capillary bed during systole; this affects the amount of light reflected back to the sensor, and a waveform is obtained. There are two types of peripheral monitors. The first is a cutaneous blood flowmeter, which detects the Doppler frequency shift of reflected light and thus measures blood flow through the capillary bed. The second is a pulse oximeter, which measures the attenuation of transmitted laser light. Two different wavelengths of light (eg, 650,805 nm) are used in addition to proper calibration to determine the percent oxygenation of the blood. Peripheral gating is convenient and is suitable for imaging the brain and vessels away from the heart.

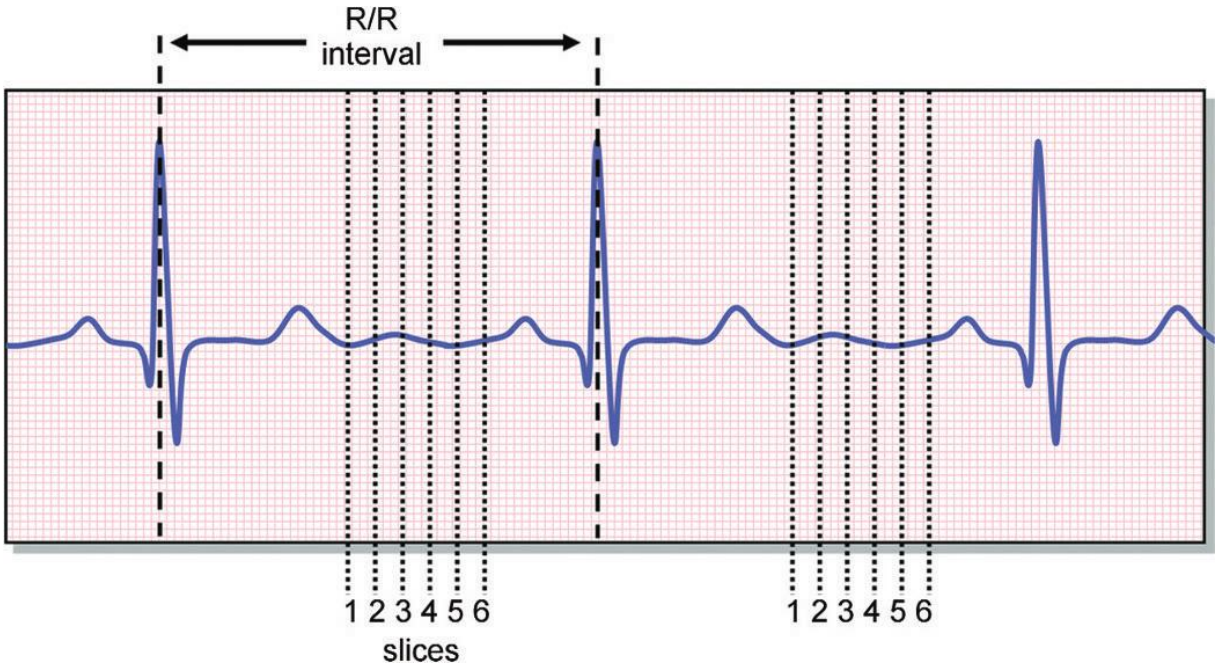

Figure 11: Slice acquisition with ECG-gated sequence. Each slice is obtained at the same phase of the cardiac cycle (65).

2.4.9.2: Limitations

There are delays in pressure wave propagation where a marked delay (150-500 ms) between the R wave of the ECG and the peak of the peripheral pulse occurs, so there is no synchronization and the systolic pulse is not simultaneous with the left ventricle contraction. Images acquired immediately after the trigger decrease in diastole and systole might be lost in the arrhythmia rejection period at the end of the cycle. The amount of delay depends on the position of the probe. Moreover, the wave peak detected is broader than those detected with ECG, resulting in inaccuracy in the triggering time (71).

3-Materials and Methods

3.1: MRI Scanners

Three MRI scanners were used for conducting measurements of this research work. These systems are produced by Siemens Healthcare (Erlangen, Germany) and are suitable for flow measurements. Their details are highlighted in table 2.

Table 2: Characteristics of MRI scanners

Parameter	Trio	Vision	Skyra
Field strength	3 Tesla	1.5 Tesla	3 Tesla
Bore size	60 cm	60 cm	70 cm
System length	213 cm	160 cm	173 cm
Gradient strength	45mT/m @ 200T/m/s	30 mT/m @ 125 T/m/s	45 mT/m @ 200 T/m/s
Slew rate	200 T/m/s	125 T/m/s	200 T/m/s

3.1.1: Magnetom Trio

The Trio is a 3T MRI scanner. Its magnet offers good homogeneity and signal stability. It was used to scan the first and second phantoms.

3.1.2: Magnetom Vision

The Vision is a 1.5T MRI scanner used for clinical and research purposes. It was used to scan the third phantom.

3.1.3: Magnetom Skyra

The Skyra is a 3T MRI scanner used for clinical and research purposes. It was used to scan subjects involved in this study (72) .

The experimental setup consisted of flow phantoms simulating blood flow through blood vessels. Three types of phantom tubes were scanned with the phase-contrast MRA (PC) sequence. The MR phase-contrast technique quantifies and displays flow volumes. The sequence uses a space-selective radiofrequency pulse followed by flow-sensitizing gradients with an echo planar readout.

3.2: Phantom

3.2.1: First phantom

To determine the influence of various MR parameters on the phase behavior of flow, serial measurements were conducted for a straight cylindrical tube with a diameter of 8 mm. The structure of the phantom is shown in figures 12 and 13. This tube was connected to a continuous pump that was pumping a mixture of water and gadolinium. To estimate the effect of stenosis on phase behavior, a semiflexible tube was inserted in the middle of the plate present in the center of the cylindrical tube and 40% to 50% stenosis was induced by applying glue to the circumference of the tube. Measurements were taken after changes in various parameters, including flip angle, direction of flow, venc factor, spatial resolutions, flow volumes, and head and body coil. Repetition time and echo time were adjusted automatically by the system itself with changes in parameters. The sequence parameters used with each phantom are shown in table 3

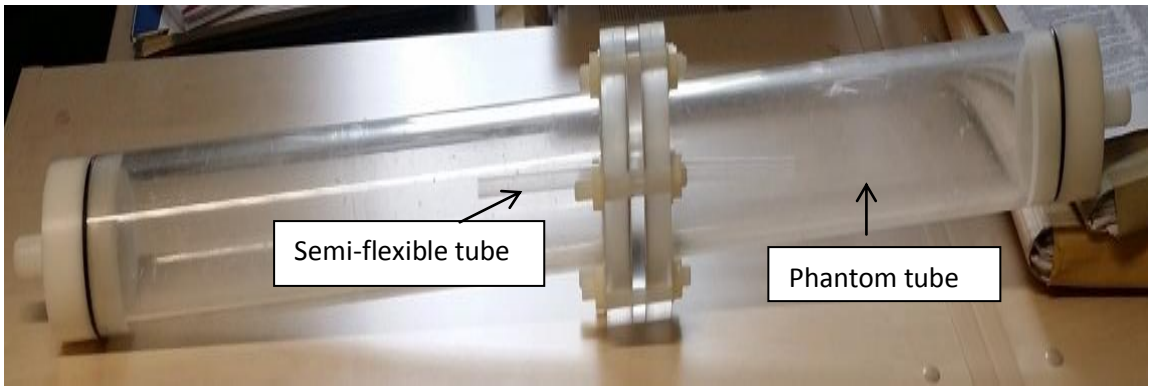

Figure 12: Shape of the 1st phantom with extensions at its ends for connection with the pump. A semiflexible tube is fixed in the middle.

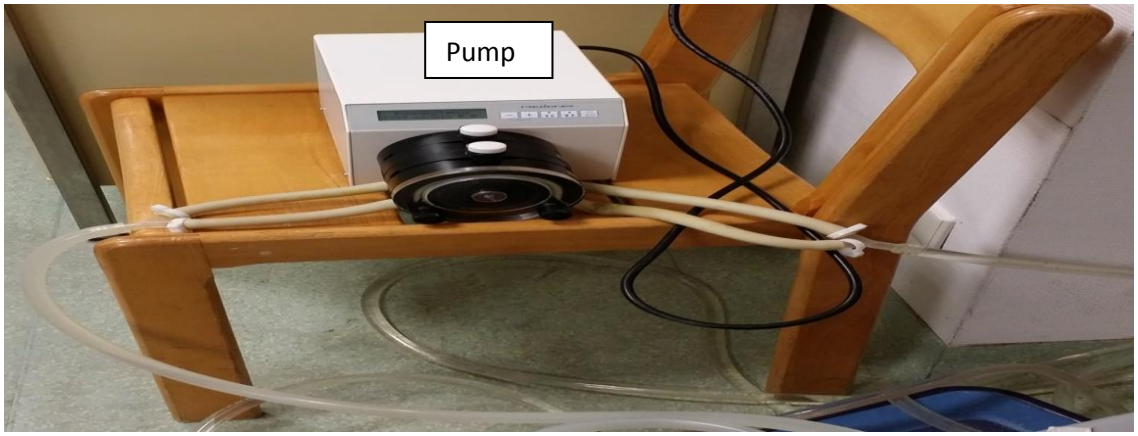

Figure 13: Connections of the first phantom to the pump.

Table 3: Sequence parameters used with each phantom.

Sequence Parameters	First phantom	Second phantom	Third phantom
TR (ms)	Adjusted	Adjusted	55
TE (ms)	Adjusted	Adjusted	3.5
Matrix	Variable	464*512	184*256
FOV (mm*mm)	Variable	110*122	115*160
Venc (cm/sec)	Variable	150	100 for 8 mm tubes 200 for 4 mm tubes
Velocity encoding	Through plane	Through plane	Through plane

3.2.2: Second phantom

To determine the influence of bending shapes and positions on the phase behavior of flow, another phantom composed of flexible plastic tube was used. Different flow volumes ranging from 100% (1200 mL) to 10% of maximum pump flow, variable bending positions and shapes, and opposite flow directions were applied. The shape of the second phantom is shown in figure 14.

Figure 14: Shape of the second phantom.

3.2.3: Third phantom

For this phantom, the measurement setup was composed of the phantom unit and a pump unit connected by 5-m long polyethylene tubes. The pump unit was composed of a centrifugal pump providing a continuous flow; it was connected to another diaphragm pump by a Y-shaped connector, and both were placed in a basin full of water. The membrane pump had a fixed displacement volume and was fed by the continuous centrifugal pump to produce physiological pulsatile flow. The flow was adjusted by 2 screws and was fixed at 0.5 L/min, resembling the physiologic blood flow in healthy internal carotid arteries. A control apparatus was used to generate the signal required for external ECG triggering. A flow sensor was mounted to a Y-shaped tube to feed the signal for the control apparatus. The control and sensor were calibrated so that current flow volumes could be read on a display. All of these structures were placed outside the magnet; only the phantom was placed inside the magnet. The structure and connections of the circuit are shown in figures 15 and 17.

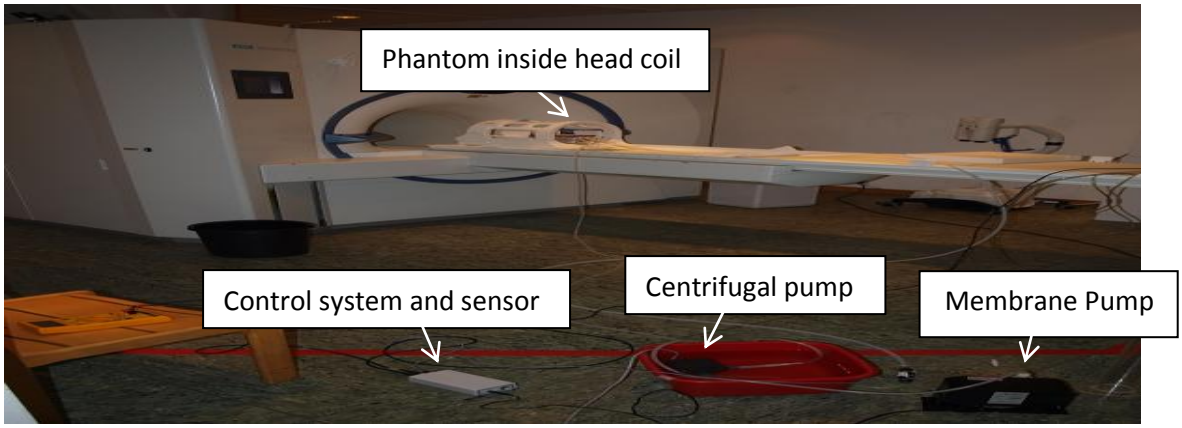

Figure 15: Connections of the phantom to pumps and signal generator.

The phantom model was constructed to mimic the normal anatomy of the internal carotid and middle cerebral arteries. The phantom consisted of 4 tubes arranged in 2 superimposed levels in the middle of acrylic plates placed in a plastic container that was filled with water (figure 16). The tubes were made of soft polyethylene. Holes were drilled through the acrylic plates so that screws could be passed through to induce stenosis (73). The degree of stenosis could be controlled by tightening the screws. In the lower level, the tube diameter was 8 mm, mimicking that of the internal carotid artery. In the upper level, the diameter was 4 mm, mimicking that of the middle cerebral arteries.

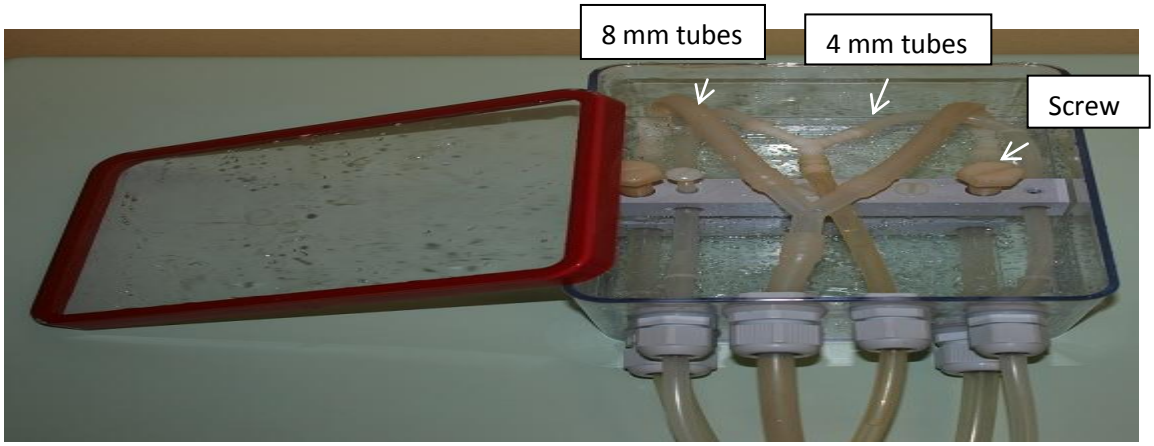

Figure 16: Shape of the third phantom.

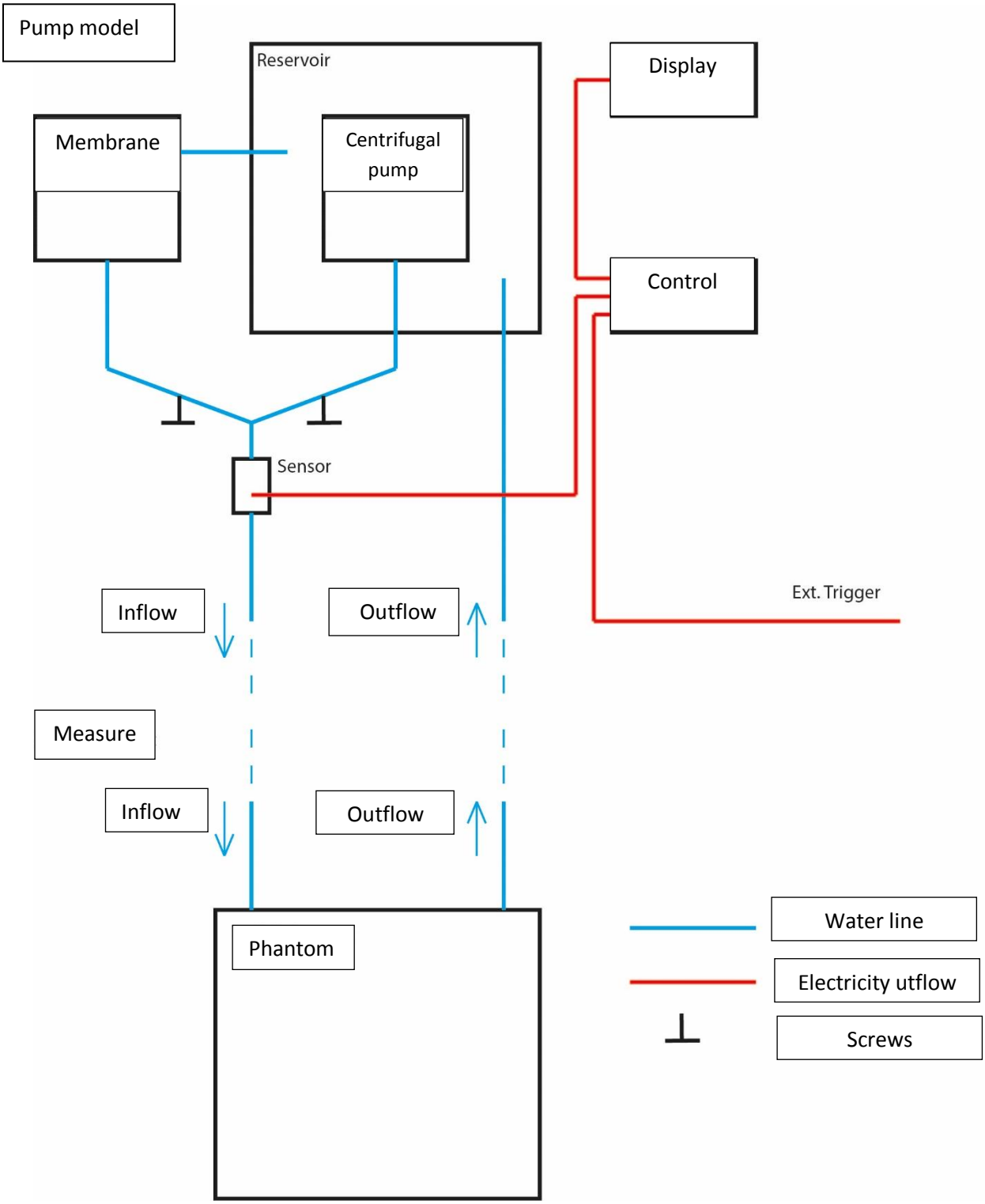

Figure 17: Block diagram showing connection of the circuit of the third phantom.

Scanning was carried out using a head coil and applying a single slice placed perpendicular to the direction of flow involving both tubes at the same time as shown in figure 18. To delineate the degree of stenosis, a static 3D gradient echo measurement

was obtained with a flip angle of 10º; serial phase contrast measurements were then obtained. Magnitude images were used to estimate the degree of stenosis, whereas phase images were used to calculate flow volumes. All scanning parameters were the same for both tubes except for venc factor; in the 8-mm tubes, a venc factor of 100 cm/s was used, whereas for the 4-mm tubes, a venc factor of 200 cm/s was used. Flow velocity is expected to be higher with a smaller diameter, so venc was adjusted to prevent a phase jump. Scanning began with full stenosis in one limb and with the other limb remaining patent. For each measurement, a half screw turn was used to decrease the degree of stenosis. The degree of stenosis was later calculated in Matlab.

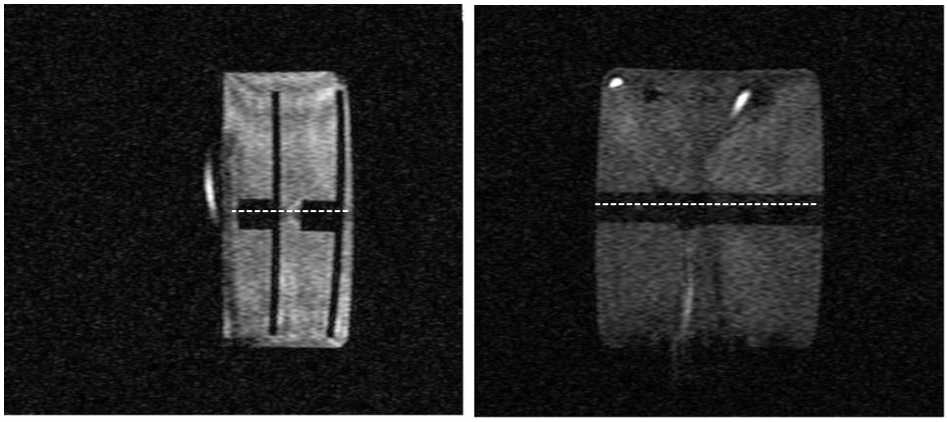

Figure 18: Scanning plan for phantom tubes in sagittal and coronal planes after 3D acquisition.

3.3: Subject Measurements

This study included volunteers and patients who were scanned between September 2014 and August 2015 after the study had been approved by the University of Tuebingen Ethical Committee. Informed consent was obtained from all study participants.

3.3.1: Volunteers

Twenty-seven volunteers (12 men, 15 women) ranging in age from 23 to 80 years were scanned.

Inclusion criteria:

Candidates were required to be in good health, aged 18 to 80 years, and able to make decisions and provide consent.

Exclusion criteria:

Patients with metal in the body, implants in the body, large tattoos, piercing jewelry,

braces, retainers, or wires were excluded. Patients who were pregnant or suffered from claustrophobia were also excluded.

3.3.2: Patients

Fifteen patients (8 men, 7 women) ranging in age from 45 to 80 years were scanned.

Inclusion criteria:

Patients with carotid or middle cerebral artery stenosis who were able to make decisions and provide consent were included in the study.

Exclusion criteria:

Patients with metal in the body, implants in the body, large tattoos, piercing jewelry, braces, retainers, or wires were excluded. Patients who were pregnant or suffered from claustrophobia were also excluded.

3.3.3: Scanning Protocol

All subjects underwent a phase-contrast QMRA examination performed on a 3T Siemens Skyra Magnetom in the Department of Diagnostic and Interventional Neuroradiology, University Hospital Tubingen. The standard 20-channel head coil or a dedicated 32-channel head coil was used.

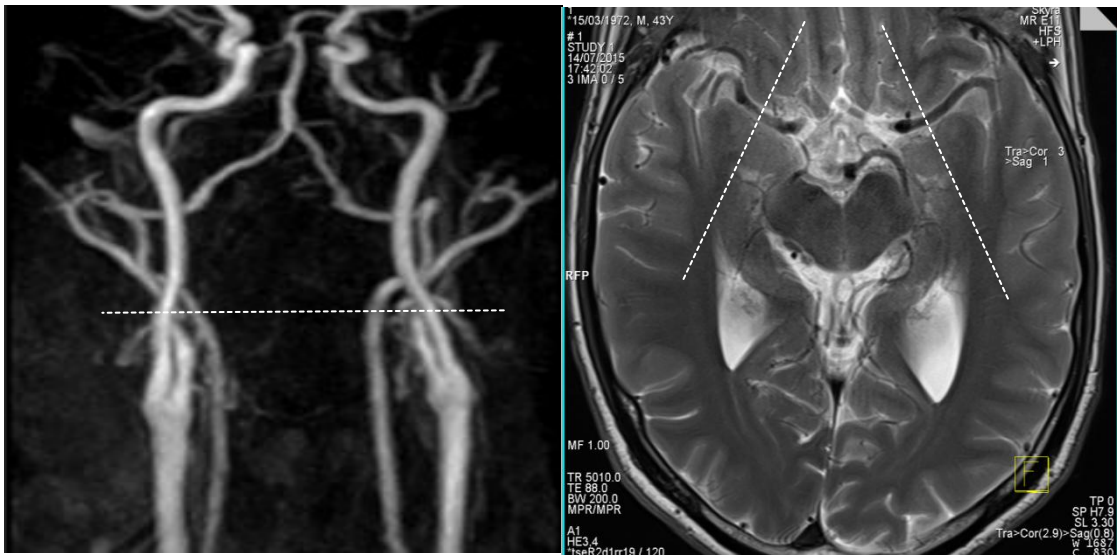

A) B)

Figure 19: Scanning plan for internal carotid artery (A) and both middle cerebral arteries (B).

Twenty-seven volunteers were examined first with a scout measurement and a T2 multislice measurement for the localization of carotids and middle cerebral arteries. A 3D MRA TOF of the head was obtained with the following parameters: TR/TE: 22/3.73

ms, flip angle: 18°, FOV: 177.19 mm, matrix: 256 x 256 mm, and section thickness: 0.6 mm. These images were used to reconstruct a 3D surface rendering of the vasculature, which was used to determine the scan plane perpendicular to the vessel of interest. In scans of the internal carotid artery, a single slice was placed, as shown in figure 19A. In scans of the middle cerebral artery, 2 slices were placed perpendicular to each artery, as shown in figure 19B, and cardiac gated phase contrast of the selected vessels was then performed with the following parameters: TR/TE: 43.84/6.94 ms, flip angle: 15°, FOV: 150 mm, matrix: 179 x 256 mm, slice thickness: 0.5 mm, and venc: 100 cm/s in the through-plane direction; for carotids, venc = 200 cm/s was used. Two volunteers were scanned with varying spatial resolutions (1 mm, 0.9 mm, 0.6 mm, 0.5 mm), and different velocity-encoding directions were assessed in one volunteer.

To estimate the effect of hand movement on middle cerebral arterial blood flow, a volunteer was scanned twice at rest and then with right hand movement followed by left hand movement. For patients, the degree of stenosis was obtained from conventional MRA scans performed by a neurointerventionalist blinded to flow measurements on QMRA.

3.3.4: Data Analysis

3.3.4.1: Matlab

Measurements with the described phase-contrast sequence provided two images, a magnitude image and a phase image. A code created with Matlab (Mathworks Natick, MA, USA) was used to analyze and quantify flow using data from the phase images. The process of analysis involved defining the artery of interest. The phase value of each pixel was defined through the cardiac cycle, and the velocity of each pixel was calculated; the mean flow and velocity of the entire vessel were then calculated.

3.3.4.2: Siemens Argus flow

Siemens Argus flow (Siemens Healthcare, Erlangen, Germany) is an automated tool used to analyze blood flow. This tool is integrated into the workstation software of Siemens Magnetom scanners. In this study, Argus flow was used to confirm the calculated flow with a Matlab code. After the desired measurement was selected, 3 image sets were displayed: flow-compensated anatomical image, a magnitude image, and a phase image. The artery of interest was identified manually and a flow report was

created; this report included the mean flow, peak velocity, mean velocity, and ROI area values (displayed in a separate window).

3.3.4.3: Siemens software Syngo

Siemens Syngo (Siemens Healthcare, Erlangen, Germany) is an automated user-friendly tool for displaying images and is integrated into the scanner workstation. This tool was used to calculate mean phase values in the first two phantoms.

4-RESULTS

4.1: Phantom

4.1.1:First Phantom

We found that there was a phase value even with no flow, as shown in figure 20. Therefore, we subtracted the phase value of the background in our future measurements.

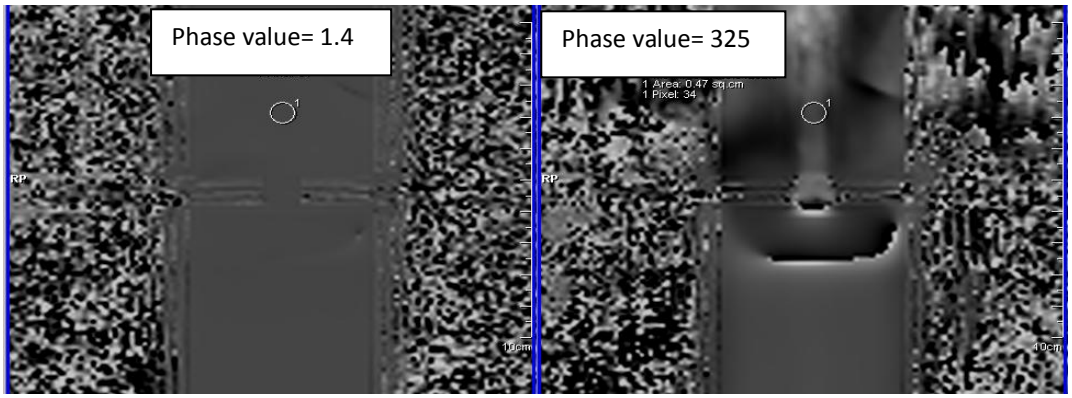

(a) (b)

Figure 20: phase values at rest (a) and with flow (b).

4.1.1.2: Different flow volumes in patent and stenotic tube

In the patent tube, phase values increased as flow increased, showing a linear relationship (figure 21).

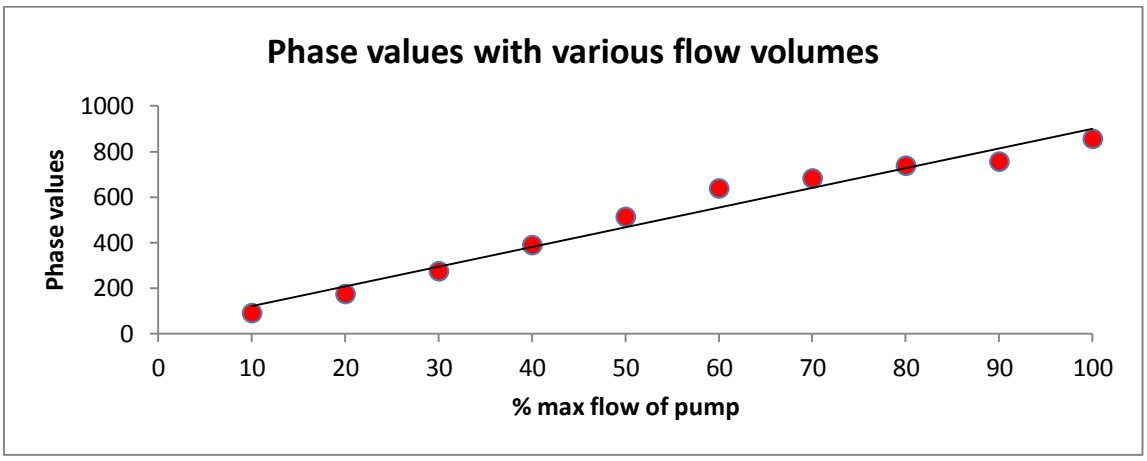

Figure 21: Phase values with various velocities and no stenosis.

In the stenosed tube, phase values were higher and there was a disruption of the linear relationship between increasing flow and phase values (figure 22).

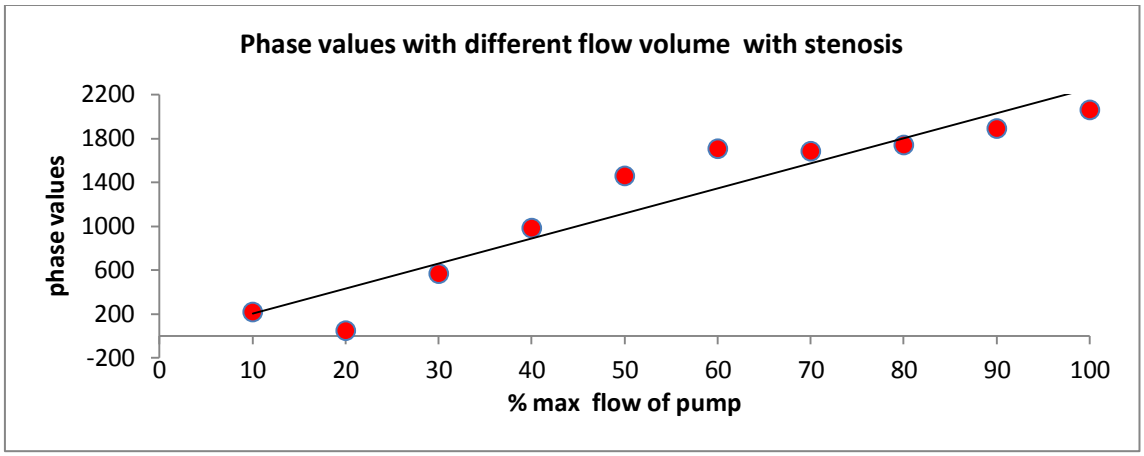

Figure 22: Phase values with various velocities in stenotic phantom.

Conclusion

Stenosis had an influence on the phase values of various flow volumes, disrupting the linear relationship between increasing flow rates and phase values. Measurements should be obtained away from the stenosis for accurate estimation of flow phase values.

4.1.1.3: Type of coil

When comparing calculated phase values using body and head coils, the linear relationship was preserved with both coils, as shown in figure 23.

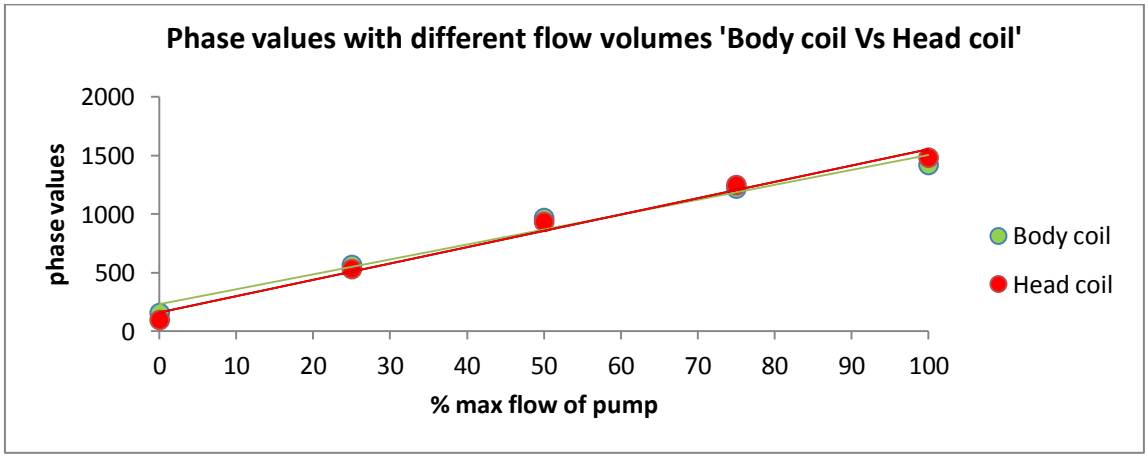

Figure 23: Phase values with various velocities using a body coil (blue circle) and head coil (red circle).

4.1.1.4: Stenosis

Measurements were performed without flow for better delineation of the stenosis shape. Stenosis induces changes in flow pattern; phase values are higher opposite stenosis (figure 24), and there is disruption of the normal smooth pattern of normal flow. An irregular flow pattern with phase jump was seen in 40-50% stenosis cases.

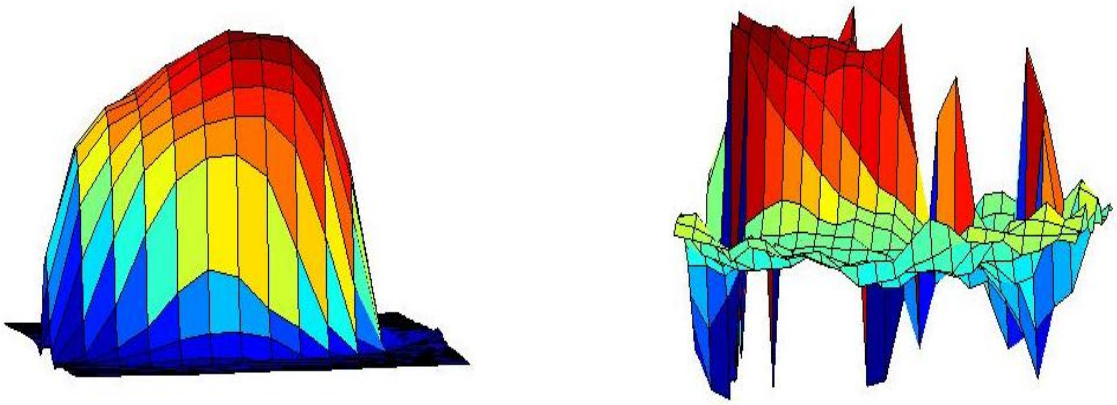

a) Flow profile in a patent tube b) Flow profile with stenosis

Figure 24: Flow pattern in patent and stenotic phantom tubes.

The flow profile changes with stenosis. Flow-related artifact is seen opposite the tube with opposite signal intensity to that of flow; furthermore, a change in the phase encoding direction changes the orientation of the artifact (figure 25).

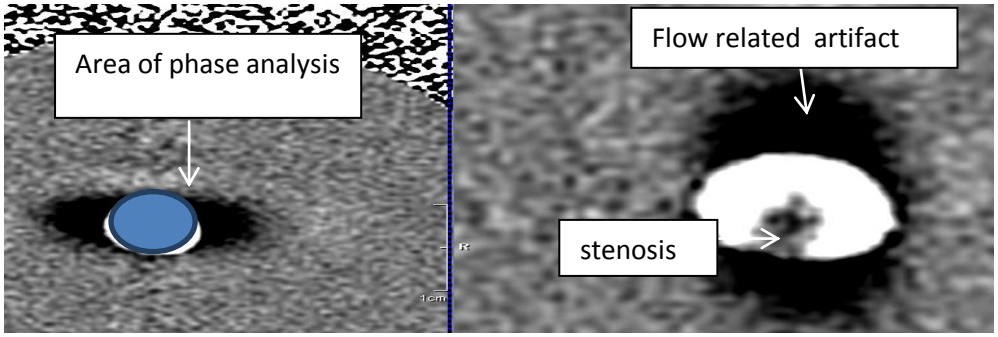

a) b)

Figure 25: Flow-related artifact in stenotic phantom tubes. A change of direction of the artifact is seen with a change in the phase encoding direction. In tube (a), the direction was from head to feet; in tube (b), the direction was from right to left.

Second Phantom

The objective of these measurements was to determine the influence of kinks in the phantom on stenosis.

4.2.1: Flow in response to tube bending in stenotic phantom

The flow pattern changed with a kink applied 25 cm from the isocenter in the direction of the head, as shown in figure 26.

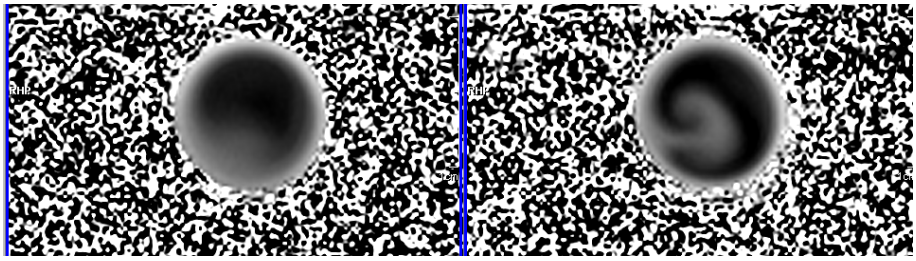

a) b)

Figure 26: Flow pattern in straight (a) and kinked (b; kink located 25 cm from isocenter) tubes.

Phase values at the center of the phantom were higher when a kink was applied, as shown in figure 27

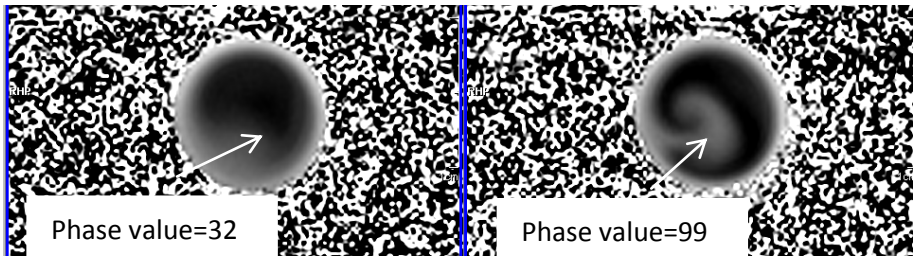

a) b)

Figure 27: Phase values in straight (a) and kinked (b; kink applied in the direction of the head) tubes.

As the shape and position of the kink changed, the phase values also changed, as shown in figure 28 (kink applied 75 cm from the isocenter once in the direction of the feet and

once in the direction of the head). The closer the kink was to the isocenter, the higher the phase value.

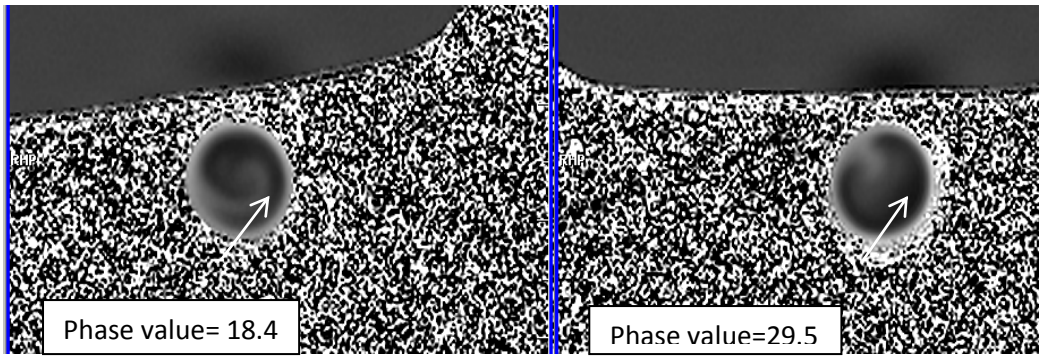

a)-Cephalic kink b)-Caudal kink

Figure 28: Phase values with different kink positions. In tube (a), the kink was applied toward the head; in tube (b), the kink was applied toward the feet.

Conclusion

The flow profile was inconsistent and inhomogeneous; with this strong deviation of phase values from expected behavior, it was not possible to identify characteristic flow profiles with various stenoses. The flow profile varied with modifications of the shape of the tube, either from bending or from the application of artificial stenosis. Some offsets of phase values were present depending on the sequence parameters. For these reasons, we chose to conduct experiments using a third phantom to estimate the influence of different degrees of stenosis on flow.

4.1.3:Third Phantom

When assessing the shape of the stenosis, we found that dynamic measurements demonstrated vibration artifact. Thus, we used static measurements with a small flip angle (10º), which offered better quality for delineation of the shape of the stenosis (figures 29 and 30). Flow volumes were measured at 4 cm before and after the stenotic segment and were found to be equal.

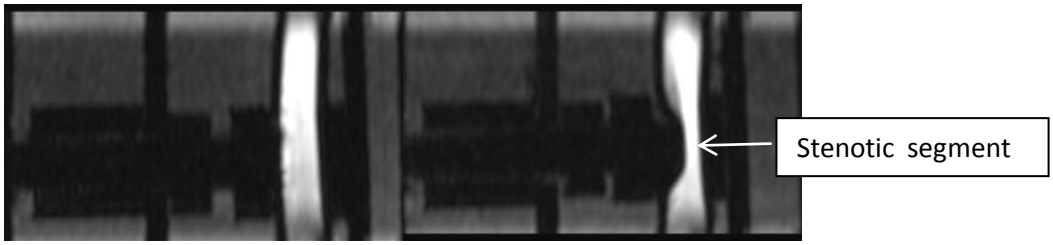

Figure 29: Phantom tube scanned with TOF, flip angle 25º, with dynamic flow.

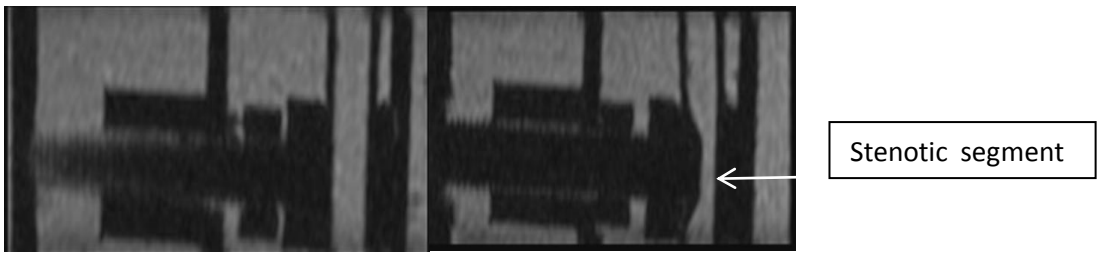

Figure 30: Phantom tube scanned with TOF, flip angle 10º, with no flow.

4.1.3.1: Flow behavior in 8-mm tubes

In high grades of stenosis, it was difficult to accurately measure the distance of the stenotic segment because of the low signal of water and dark signal of the surrounding plate and screw. With a Matlab code, we calculated the distance from the top of the screw to the lower plate in full patency and used this as a reference to calculate the distance moved by the screw as it induced stenosis, allowing for accurate calculation of the tube's patency (figure 31).

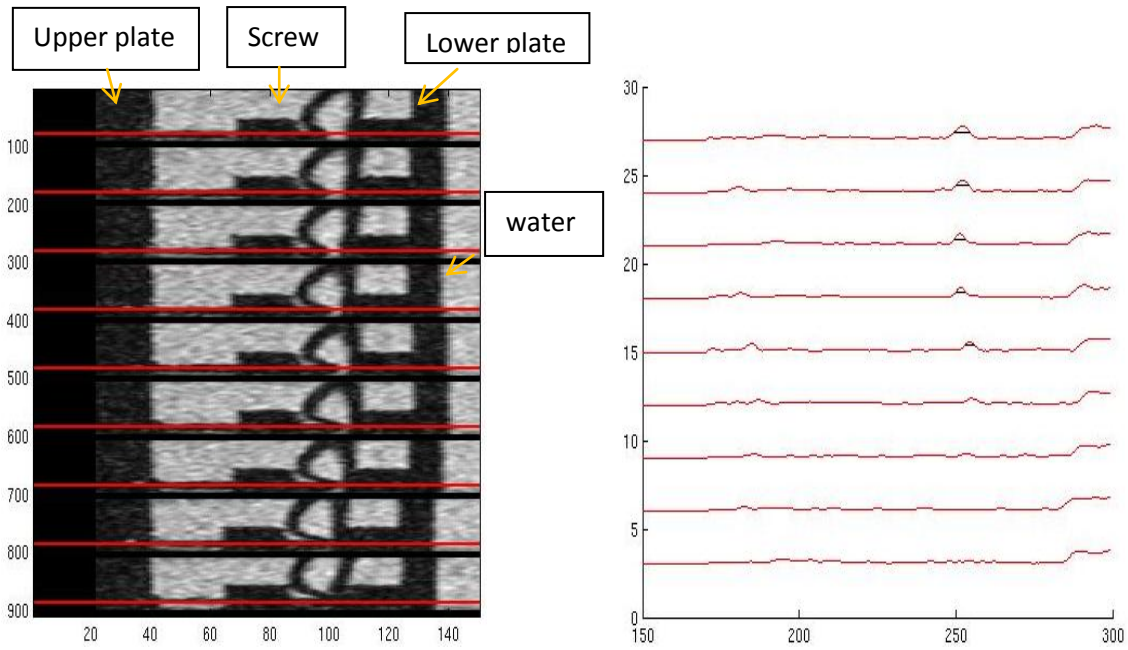

Figure 31: Estimation of the degree of stenosis in phantom tubes.

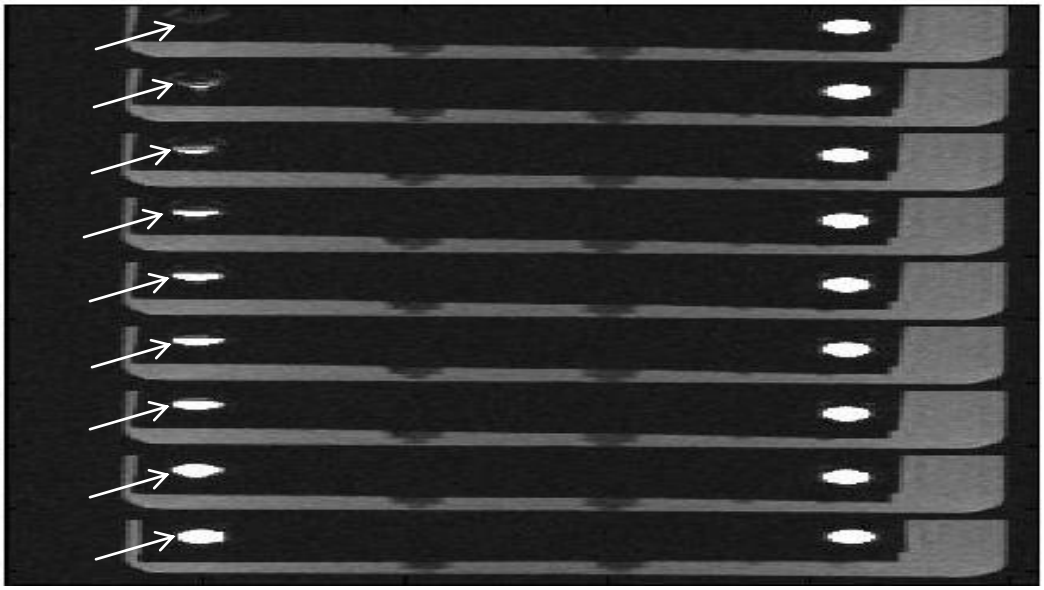

Figure 32: Flow in 8-mm tubes. The left is fully patent; the right shows varying degrees of stenosis (arrows).

With increases in the degree of patency of the stenotic tube, the mean phase values increased in the stenotic tube but decreased in the patent tube until becoming become equal in fully patent tubes (figure 33).

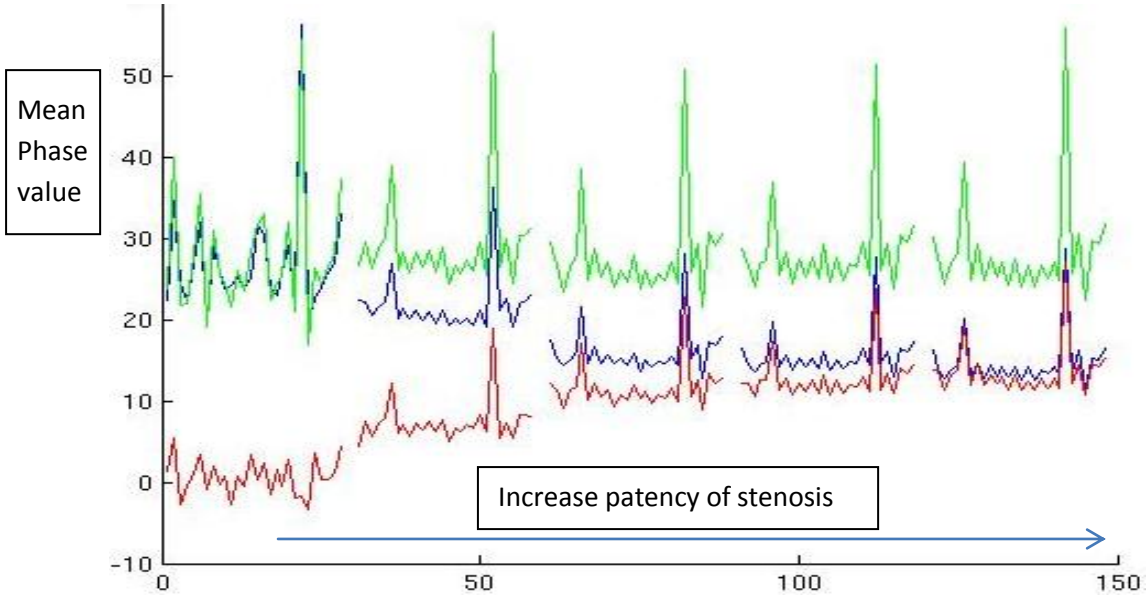

Figure 33: Mean phase values with varying degrees of stenosis in 8-mm tubes. Green spikes represent total flow, red spikes represent the stenotic tube, and blue spikes represent the patent tube. Each column of spikes represents one cycle of 1-s duration.

The flow was stable with different degrees of stenosis up to 75%, at which point flow decreased linearly until it vanished with full stenosis (figure 34).

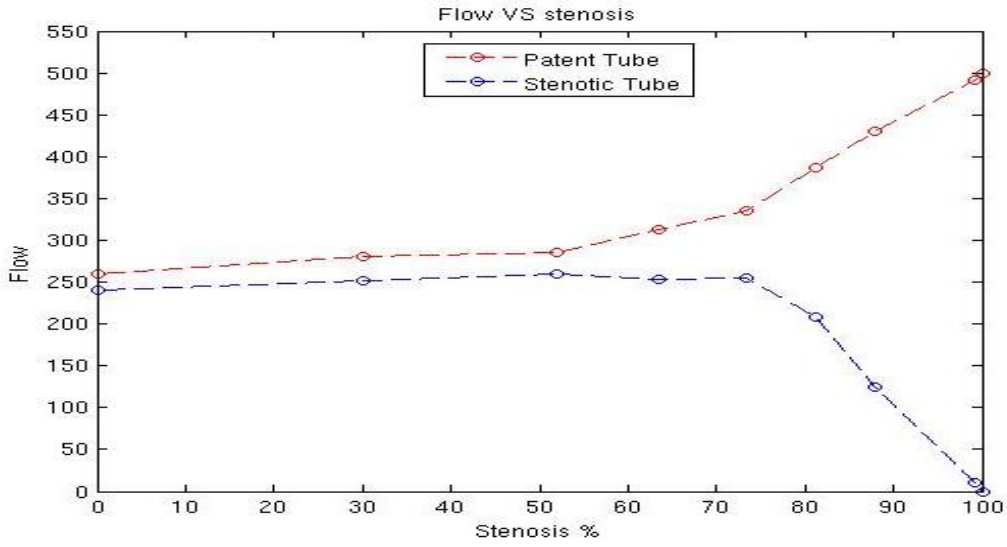

Figure 34: Correlation between the amount of flow and the degree of stenosis in 8-mm tubes. The red dotted line represents flow in the patent tube; the blue dotted line represents flow in the stenotic tube.

4.1.3.2: Flow behavior in 4-mm tubes

The same measurement was carried out in 4-mm tubes. The appearance of the stenotic limbs can be seen in figure 35.

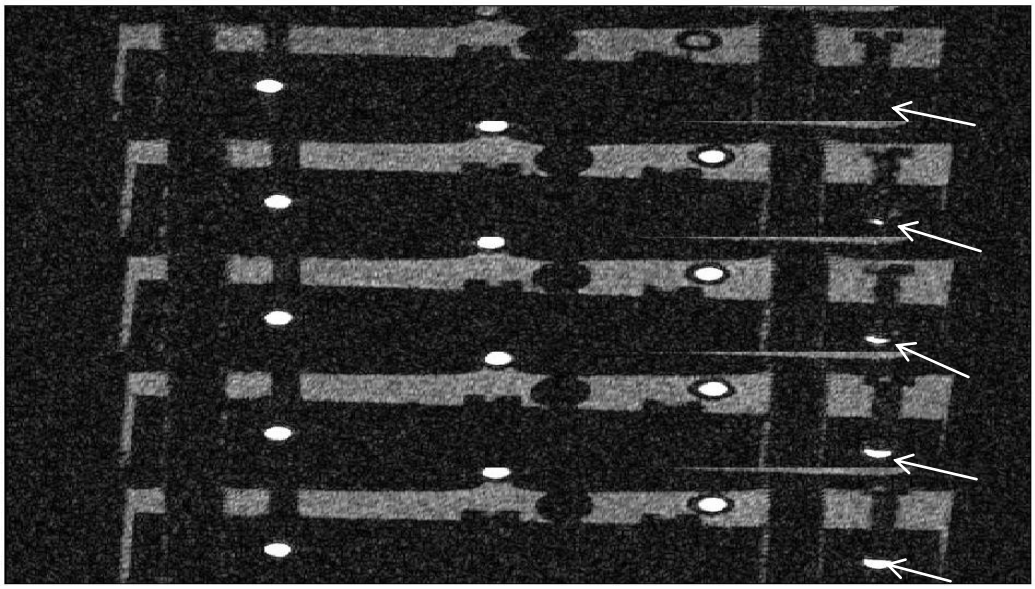

Figure 35: Flow in 4-mm tubes. The right is fully patent; the left shows varying degrees of stenosis (arrows).

Phase values increased in the stenotic limb and decreased in the patent limb, as shown in figure 36. The flow was stable with varying degrees of stenosis up to 65%, after which flow decreased linearly in the stenotic limb until it vanished with full stenosis (figure 37).

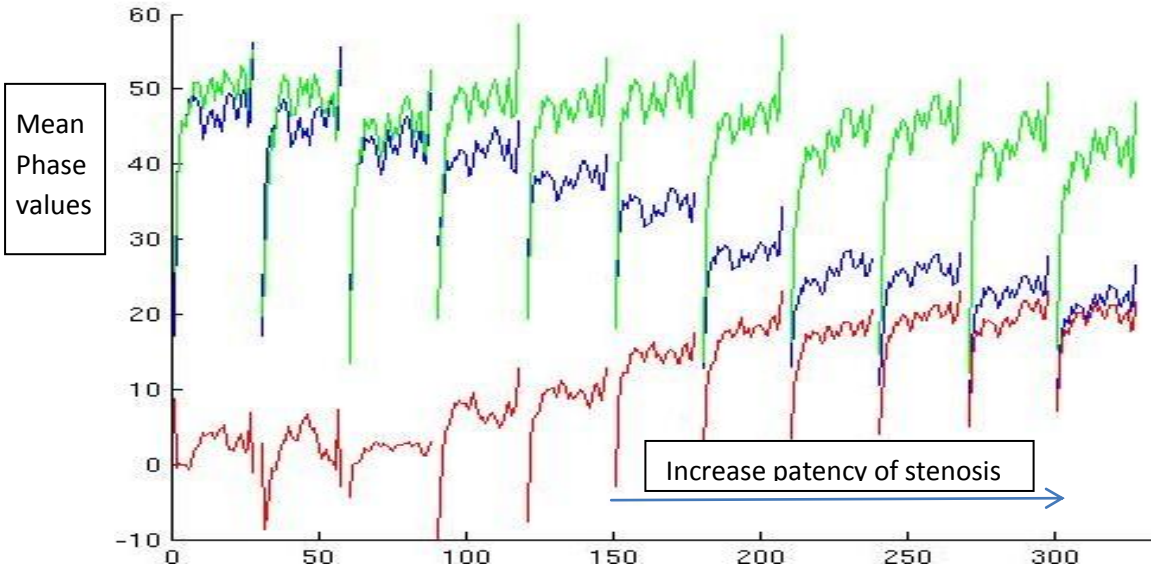

Figure 36: Mean phase values with varying degrees of stenosis in 4-mm tubes. Green spikes represent total flow, red spikes represent the stenotic tube, and blue spikes represent the patent tube. Each column of spikes represents one cycle of 1-second duration.

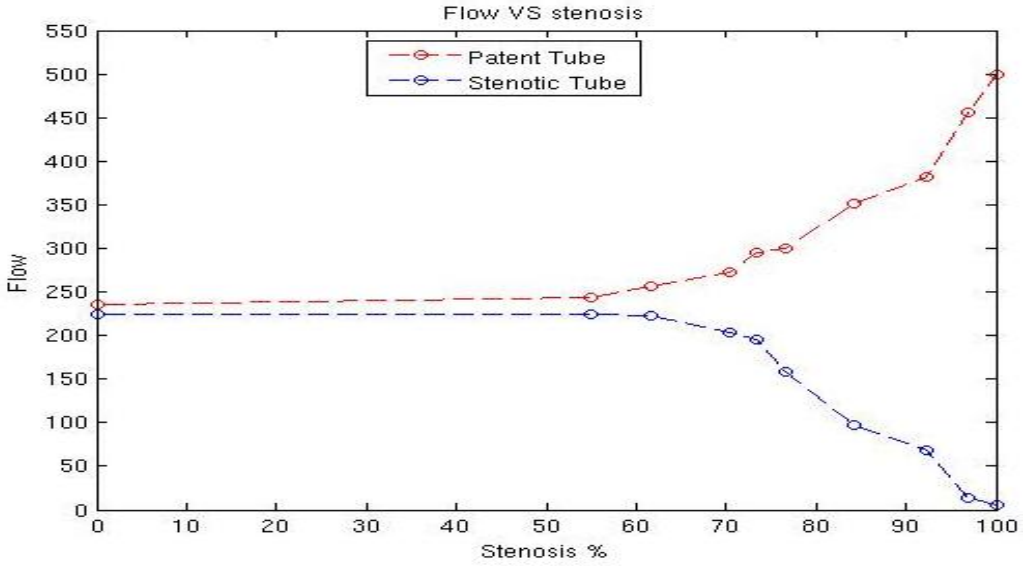

Figure 37: Correlation between the amount of flow and the degree of stenosis in 4-mm tubes. The red dotted line represents flow in the patent limb; the blue dotted line represents flow in the stenotic tube.

4.2: Subjects

4.2.1: Findings in Volunteers

We found that the through-plane venc encoding direction was the only direction in which the artery could be visualized; furthermore, 0.5 mm provided the best spatial resolution, offering accurate delineation of the artery boundaries and enabling adequate flow quantification. Scanning of patent and stenotic ICAs and MCAs was performed; the flow profiles in patent and stenotic MCAs are illustrated in figure 38

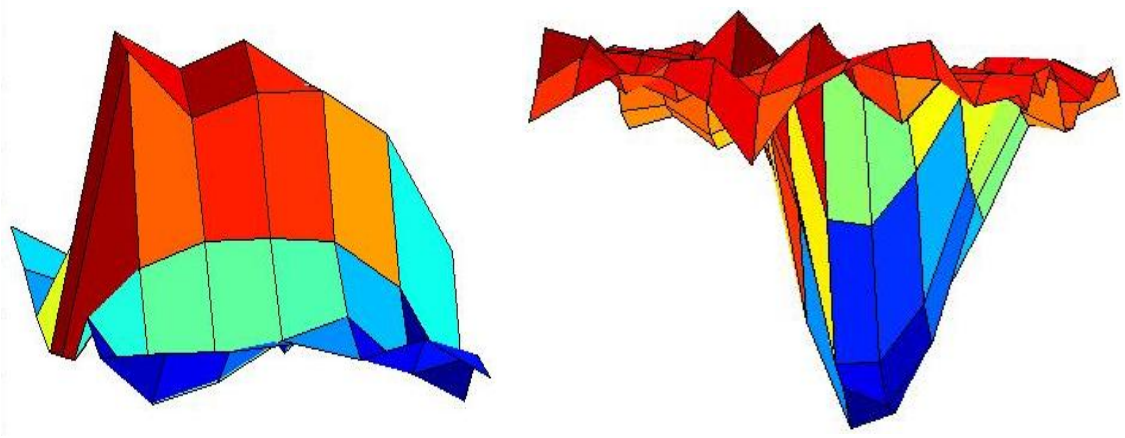

Figure 38: 3D diagram of flow profiles in the MCA. (a) Patent right MCA; (b) Stenotic left MCA.

For flow quantification, subjects were scanned and an ROI involving the artery of interest was defined. The phase value of each pixel was then calculated with Matlab. Mean phase values of the whole artery were estimated, and mean velocity and mean flow of the desired artery were calculated. The steps of analysis with Matlab are shown in figure 39. Flow volumes, velocities, and differences between sides (calculated as flow on right side – flow on left side/mean [right + left flow]) were calculated for the middle cerebral, carotid, and vertebral arteries in volunteers (table 4).

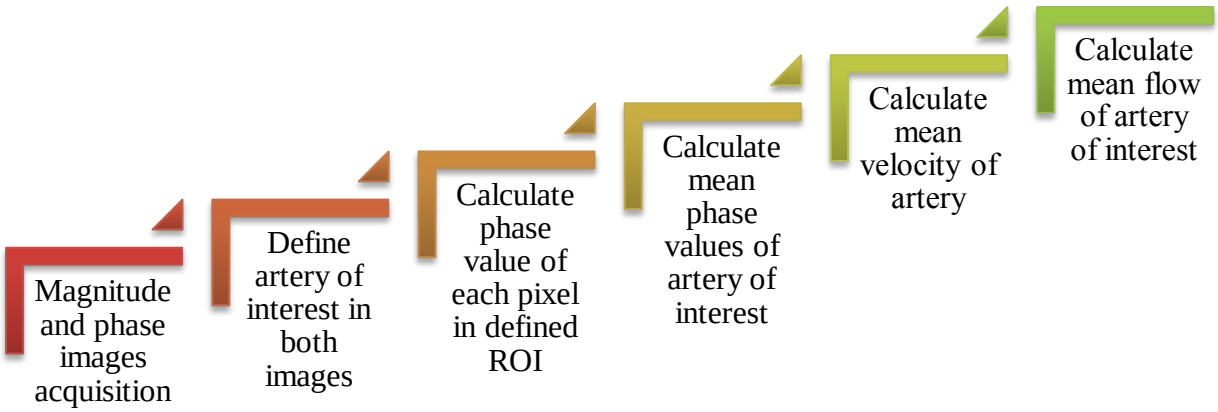

Figure 39: Diagram showing the steps of flow analysis using Matlab.

Table 4: QMRA findings in volunteers:

Artery	**Mean right flow** (mL/min)	**Mean left flow** (mL/min)	**Range of difference** (Right flow – left flow/mean flow)	**Mean difference** (Right flow – left flow/mean flow)	**Mean of absolute value of difference**
MCA N=21	146.6 ± 33.5	140 ± 33.6	–11% to 11%	+4.1%	6% ± 3%
ICA N=6	236.5 ± 73.1	228.8 ± 69.9	–11% to 11%	+3.6%	7% ± 4%
VA N=3	91 ± 10.5	94.6 ± 14.2	0% to 11%	+3.6%	3.6% ± 6%

We found that the difference in flow for both MCAs and ICAs ranged from –11% to 11%. There was a difference between the mean difference in flow and the mean of the absolute value of difference because some subjects had higher flow on the left side. A representation of the difference in flow in relation to age is shown in figure 40.

.

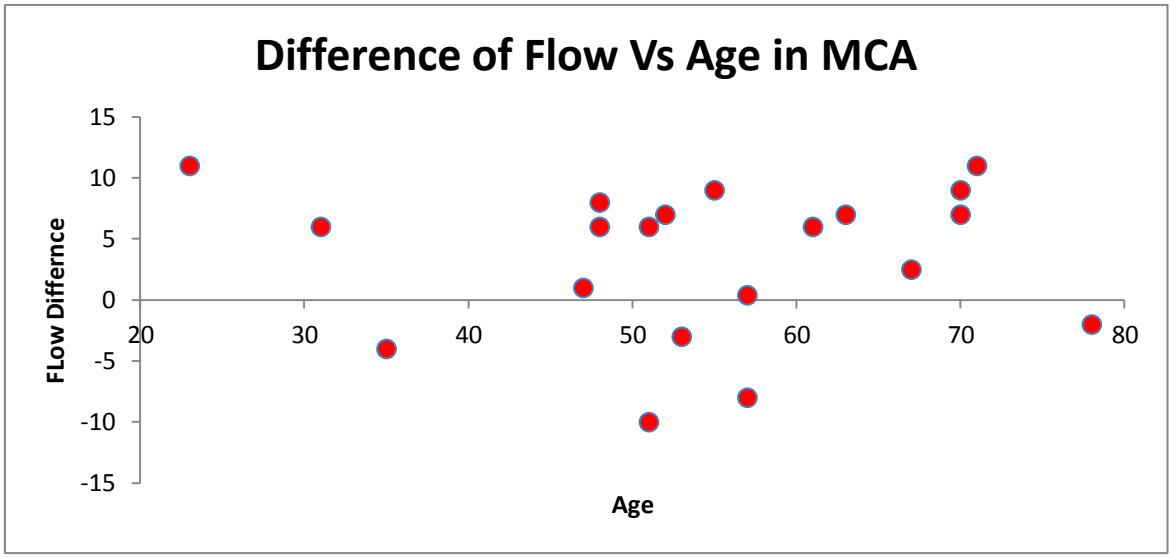

Figure 40: Percentage difference in flow between both sides vs age for MCA. Difference was calculated as (right flow – left flow/mean flow between both sides) × 100.

Conclusion

There was a difference in flow between paired arteries; this difference was independent of age but varied according to the health status of each subject.

4.2.1.1: Effect of hand movement on middle cerebral artery flow

Two measurements were performed in a volunteer on two different occasions at rest, with right hand movement, with left hand movement, and at rest again. Flow was calculated for these conditions (figures 41 and 42). We expected that with hand movement, there would be an increase in flow in the contralateral middle cerebral artery, as was seen in a previous study by Matteis et al (75). However, we could not define a systematic influence of hand movement on blood flow in the middle cerebral artery. Additionally, we observed high variability in flow volumes in the same artery with the same task; no systematic pattern of flow augmentation was found.

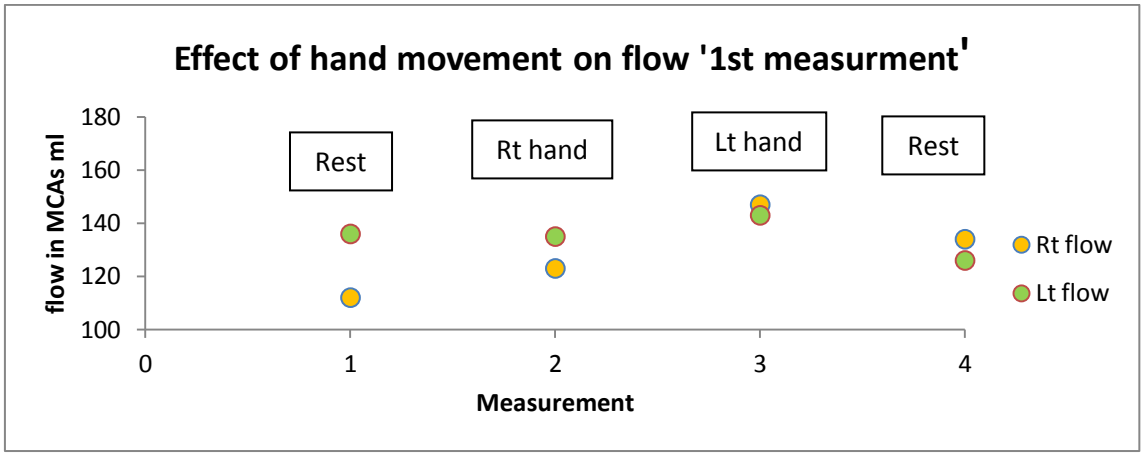

Figure 41: Flow values in middle cerebral arteries in response to hand movement (first measurement).

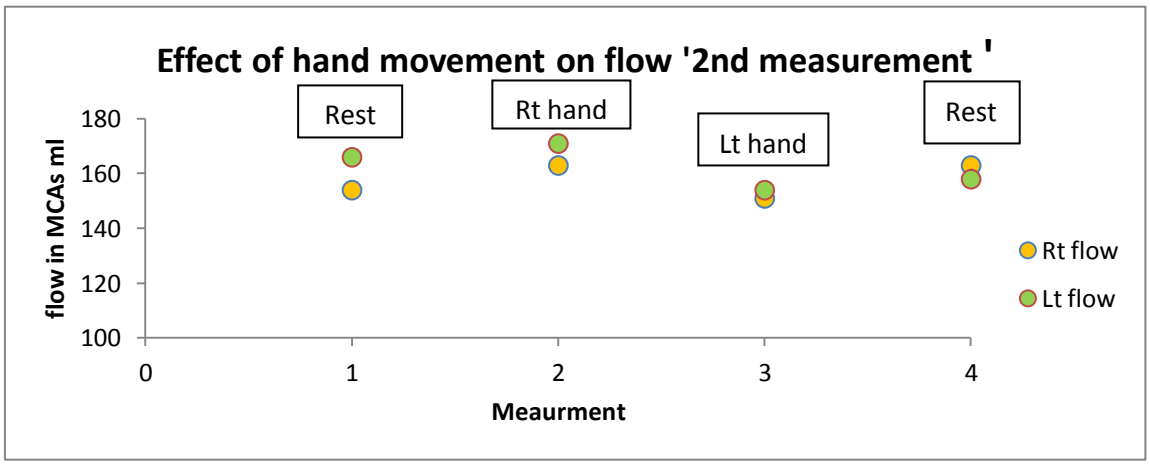

Figure 42: Flow values in middle cerebral arteries in response to hand movement (second measurement).

4.2.2: Findings in patients

A total of 11 internal carotid arteries, 3 middle cerebral arteries, and 5 vertebral arteries were scanned in 13 patients. For each patient, flow, mean velocities, and the difference between sides in flow (flow in patent artery – flow in stenotic artery/mean flow in both arteries) were calculated (table 5). We found that there was a difference between flow on both sides; this difference was >16% and was higher than the maximum difference observed in our volunteer subjects. In 3 patients, there was increased velocity on the stenotic side.

Table 5: Vessel flow rates and velocities in patients with stenosis.

No	**Age**	**Rt flow** (mL/min)	**Lt flow** (mL/min)	**Difference** (Rt flow-lt flow/mean flow)	**Rt velocity** (cm/s)	**Lt velocity** (cm/s)	**MRA findings**
Internal Carotid Artery							
1	45	216	254	-16,1	35,8	39,9	Rt 50%
2	66	358	304	16,3	20,9	22,4	Lt 40%
3	80	226	151	39,7	43,4	22,1	Lt 40%
4	63	242	86	95,1	45,7	34,6	Lt 90%
5	70	208	313	-40,3	35,3	32,5	Rt 40%
6	51	76	308	-75,3	43,1	66,1	Rt 70%
7	71	177	209	-16,5	26,7	18,8	Rt 30%
8	70	187	284	-41,1	25,4.	32.9	Rt 60%
9	73	215	281	-26,6	43.1	34.9	Rt 40%,Lt ICA stent
Internal carotid artery with stenotic left MCA							
1	58	244	169	36,3	33,3	32,3	Lt MCA 70%
Middle meningeal artery							
1	62	183	94	51	49,8	36	Lt 95%
2	72	170	39	77	62,5	26,2	Basilar artery stent, Lt 40%
3	58	145	39	73	54,4	48,9	Lt 70%
Vertebral artery							
1	58	24	38	-45	9	9	Lt VA stent
2	70	114	0		25.9	0	Occluded Lt VA
Vertebral artery with internal carotid artery stenosis							
1	58	87	52	50	31	26,7	Lt MCA 70%
Stented left vertebral artery							
1	58	24	38	-36	9	9.2	

Patients had reduced flow in stenotic vessels compared to the other side and also compared to mean flow in our volunteer subjects; some patients had increased flow in patent arteries (figure 43).

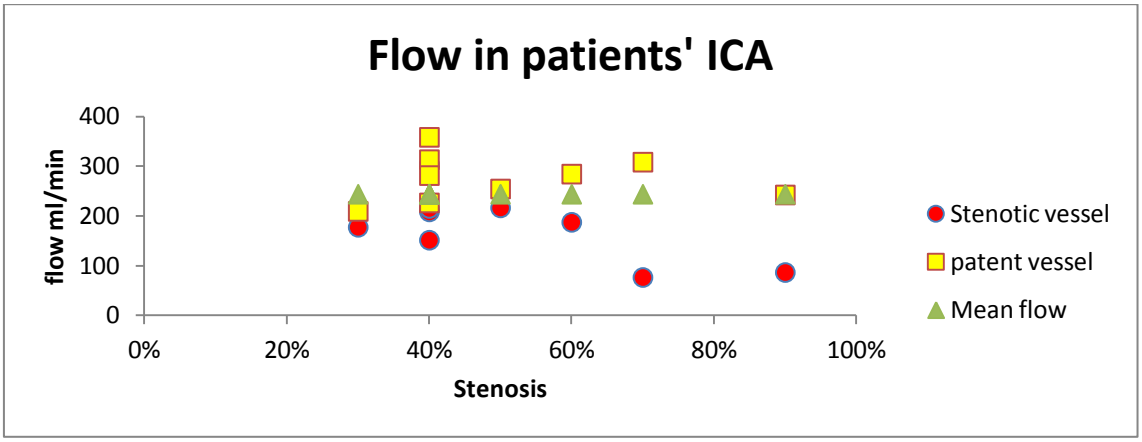

Figure 43: Flow in patients' ICA on both sides in correlation with the degree of stenosis by conventional MRA.

QMRA results demonstrated reduced flow on the exact side detected with conventional MRA, with a strong correlation between QMRA and conventional MRA (R^2 =0.7942). The percentage of flow difference between sides varied with the degree of stenosis. In 3 patients with a degree of stenosis of more than 60% in the ICA, the difference in flow increased with the percentage of stenosis. The difference in flow between stenotic ICAs assessed with QMRA versus the degree of stenosis assessed with conventional MRA is shown in figure 44.

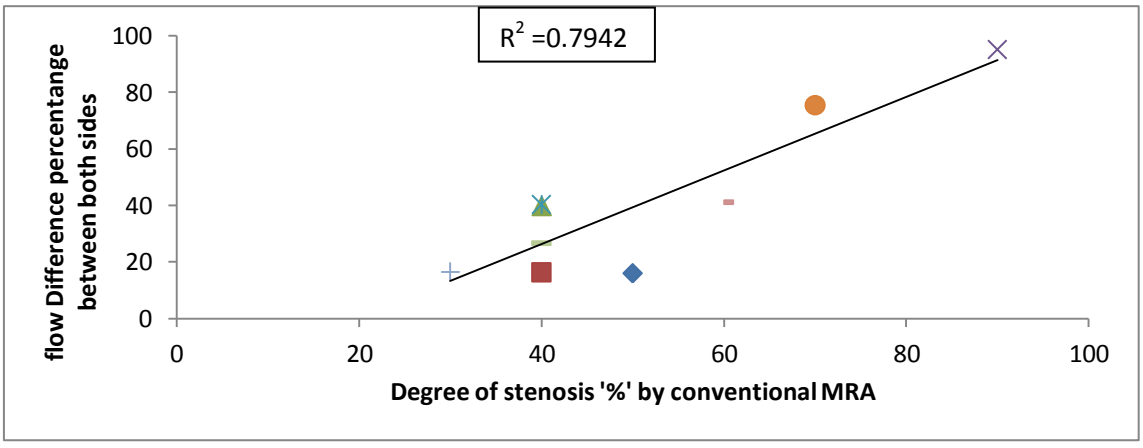

Figure 44: Percentage difference in flow between internal carotid arteries bilaterally using QMRA compared to degree of stenosis by MRA.

5-DISCUSSION

Carotid stenting has been FDA approved in 2004. The gold standard modality for evaluation of vessel and stent patency is DSA, however it possesses serious side effects such as radiation exposure, risc of neurologic ischemic complications and contrast induced nephrotoxicity. In-stent stenosis is considered to be the primary etiology of recurrent stroke in follow up period and could be retreated with either angioplasty alone or with re-stenting.

The aim of our project was to develop a new technique for the follow-up examination of patients who were treated by balloon angioplasty and stenting for symptomatic stenosis of the internal carotid artery or major intracranial arteries. Our goals were to implement and optimize sequences for quantitative MR angiography, to permit spatial and time-resolved flow encoding, estimate the flow velocity, and characterize stenosis and assessment of its degrees. Another objective was to find a relation between flow differences on both sides in healthy subjects, to set a baseline above which we might expect stenosis to obscure flow.

Ota et al reported that MIP images overestimate stenosis, as the background signal intensity conceals faint signal intensity at the stenotic region (74). Time-of-flight MRA also has limited capability for the follow-up of stenting; one study reported a decrease in the in-stent signal caused by susceptibility artifact or radiofrequency shielding artifact. The degree of artifact changed according to 2 factors: the applied MR parameters (eg, flip angle, bandwidth) and the stent type (75). In another study, Offerman et al applied various flow velocities in a pulsatile flow phantom with 50% diameter stenosis at 1.5T to evaluate the signal properties of 2D TOF (MRA). The authors found that there was signal loss after stenosis, and as the velocity increased, the sensitivity to flow artifacts also increased (76).

Multiple studies have demonstrated the accuracy and reproducibility of velocity and volumetric flow measurements obtained with phase contrast MRA. PC MRI has been evaluated in the heart and major blood vessels; in phantom studies, this modality has demonstrated high accuracy in velocity mapping of vessel models down to a 3-mm diameter (77-81). With PC MRI, the sampling plane within the vascular anatomy can be selected visually far from regions with branches or kinks. Furthermore, this modality

can simultaneously measure geometrical and fluid-dynamics data without the use of any endovascular device or contrast agent that could potentially alter the blood flow. The velocity values calculated with this technique are equivalent to those acquired with ultrasound-based techniques (82).

Phantom measurements are important in medical imaging for the validation and optimization of various parameters before these parameters are used in human subjects. In our study, we used phantom tubes to mimic, as closely as possible, the imaging appearance of the normal anatomy and its distortion by stenosis. We obtained several measurements to optimize parameters, checked phase behavior with various flow volumes, and determined the effect of varying degrees of stenosis on flow volume in anthropomorphic and nonanthropomorphic flow phantoms.

In our measurements of patent and stenotic phantom tubes, our results agreed with those of Stahlberg et al (83) regarding a nonlinear relationship between phase and velocity in stenotic phantoms with various degrees of complex flow. In straight phantoms, the linear relationship between phase and velocity was maintained.

We found that stenosis and changes in tube configuration induced changes in phase values; changes in flow pattern made it difficult to depend on phase values for velocity calculations, as no systematic phase behavior is available for various kink forms and positions. O'Brien et al similarly observed precise flow measurements (average error 1.8%) in patent tubes, whereas significant errors were found in stenotic tubes; these errors were associated with signal loss in flow-compensated magnitude images magnitude image **(**84).

For better delineation of the shape of stenosis, static measurements offered higher quality than dynamic measurements owing to the absence of moving artifacts induced by flowing fluid. In our study, when varying degrees of stenosis were applied in 8-mm tubes, flow was lower in the stenotic tube and remained stable over various degrees of stenosis until 75% stenosis was reached; at this point, flow began to decrease. This decline was linear until full stenosis was reached. When varying degrees of stenosis were applied in 4-mm tubes, a similar pattern was observed, but the decline started at 65% stenosis and continued until full stenosis was reached. According to Poiseuille's

law, 4-mm tubes offer higher resistance to flow than 8-mm tubes (equation 1) and this explains different decline starting point in both tubes

When we assessed flow volumes in subjects, mean phase values within the ROI containing the artery of interest were used to estimate flow. However, we noticed that the signal in magnitude images did not always show the whole area; therefore, we used both magnitude and phase images in flow analysis. Schubert et al investigated the effect of multidirectional velocity encoding in tortuous arteries by measuring peak velocities in 3 locations along the distal internal carotid artery with 3D 3-directional time-resolved PC and 2D 3-directional and through-plane velocity encoding PC sequences. The authors found that unidirectional encoded through-plane PC led to significant underestimation of velocity values in tortuous vessels, likely because of the complex flow pattern in these vessels and the difficulty in placing the scan plane perpendicular to the vessel axis (85). In our study, the scanned arteries demonstrated a straight course; therefore, the scan line was perpendicular to the direction of flow using a single venc encoding direction (through plane).

QMRA was used to assess cerebral blood flow (44, 86). The protocol stated with 2D TOF followed by 3D TOF. TOF images were sent to a separate workstation to produce a 3D surface rendering of the vessels using Noninvasive Optimal Vessel Analysis software (NOVA). This software also adjusted the velocity encoding according to the scanned vessel. PC-MRA was performed perpendicular to the artery of interest with a spatial resolution of 0.7 mm and 0.5 mm for extracranial and intracranial arteries, respectively. A report was generated through NOVA containing flow rate values in mL/min, and the percent difference was calculated ([right flow - left flow/mean flow] × 100). Flow volume values from 2 previous studies and our results are shown in table 6.

Amin Hanjani et al found that the total cerebral blood volume decreased by 2.6 mL/year in addition to the flow of each single vessel. Both studies demonstrated higher mean flow values in the left MCA, ICA, and VA than in the right MCA, ICA, and VA in all age groups; the flow rates decreased with age. Amin Hanjani et al also found that ICA flow was affected by the anatomy of the posterior communicating artery and posterior cerebral artery in the region of the circle of Willis (86). In our study, the percentage difference between arteries varied among healthy subjects and was independent of age.

Table 6: Comparison of our study flow results with flow results of previous studies.

	Number of Subjects	**Rt MCA flow** (ml/min)	**Lt MCA flow** (ml/min)	**Difference** (Rt flow-lt flow)/mean flow	**Rt ICA flow** (ml/min)	**Lt ICA flow** (ml/min)	**Difference** (Rt flow-lt flow)/mean flow	**Rt VA flow** (ml/min)	**Lt VA flow** (ml/min)	**Difference** (Rt flow-lt flow)/mean flow
Zhao(44)	83	145 ± 27	150 ± 31	-3.3%	252 ±52	264 ±52	-4.7 %	83± 32	96 ± 38	-14%
Amin Hanajan(86)	334	146 ± 28	159 ± 28	-10%	256 ± 50	259 ± 52	-8.5%	88± 30	100 ± 38	-12%
Our study	27	146±33	140±33	6 %	236±73	228± 69	7 %	91±10	94±14	-3.6 %

Variation in flow volumes could be attributed to the fact that the previous 2 studies had larger populations than ours, their physiological status and different method of analysis in our study. For the percent difference in MCAs, our results were close to the results of Zhao et al. The percent difference observed in the study by Amin Hanjani study et al (10%) was close to the upper limit calculated in our study (11%). For ICA, the percent difference we found was close to that observed by Zhao et al. The mean of absolute value of difference in our study (7%) was close to that observed by Amin Hanjani et al (8.5%). For VA, the percent difference was similar in the studies by Zhao et al and Amin Hanjani et al, but our results were markedly different. This could be because of the small number of analyzed VAs in our study (N=3).

We were unable to determine a systematic influence of hand movement on flow in the MCA, contrary to previous work by Matteis et al that demonstrated an increase in mean blood flow after active and passive hand movements detected with transcranial Doppler (87).

In our study , we compared our flow value results to the degree of stenosis as measured by MRA and interpreted by a highly experienced neurointerventional radiologist. QMRA demonstrated a decrease in flow in stenotic arteries compared to flow on the patent side and compared to flow in healthy volunteers. In all examined patients, QMRA demonstrated a difference in flow values between sides for ICA and MCA. For

ICA, the difference ranged from 16% to 95%; for MCA, the difference ranged from 51% to 77%. In 2 patients with stenotic ICA, stenosis affecting the corresponding vertebral artery was found. For patients with stenosis affecting the middle cerebral arteries, flow volume and velocity were decreased on the stenotic side. ICAs with stenosis showed decreased flow and velocity compared to patent ICAs, except for 3 patients who demonstrated high flow velocity; this could be attributed to the pattern of stenosis. One patient with a stented left vertebral artery demonstrated higher flow in the stented artery. Another patient with an occluded left vertebral artery demonstrated no flow with our technique. Patients demonstrated decreased flow and velocity in the diseased sites.

Our results agree with those of Shakur et al, who showed that ICA flow decreases with a higher stenosis percentage. Our study also demonstrated that the percentage of stenosis is the main predictor of ICA flow (88).

In our study, in both patients and phantom measurements, for small degrees of diameter reduction, there is no change in the flow, which could be explained by a higher flow velocity till a certain point after which there is almost linear decline of flow with increased degree of stenosis. The effect of stenosis on is different among healthy subjects compared to phantom tube owing to influence exerted by age, anatomy, physiological factors such as breathing, while in patients, other pathological processes such as coronary artery disease, hypertension would definitely affect blood flow.

6- Summary.

Stroke represents the third leading cause of death and main reason for disability worldwide. Stenosis affecting internal carotid artery due to atherosclerosis is responsible for almost 30-40 % of ischemic strokes Stenting is used to restore lumen patency. In stent stenosis occurs in 25-35% of patients. Stent related artifacts and artificial lumen narrowing are problems arise during MRI stent examination. Quantifying flow is an alternative to detect stenosis through its physiologic effect. The objective of our project was to implement and optimize sequences for spatial and time resolved flow encoding and the estimation of the flow velocity allowing for better characterizing stenosis and assessing its degrees. To achieve this objective, a phantom model mimicking normal anatomy of internal carotid and middle cerebral arteries was built composed of 8 and 4 mm tubes connected in Y-shaped form to pulsatile pump pumping 500 ml at rate 60 beat/min. Different degrees of stenosis were applied to one limb while the other remained patent. We scanned with phase a contrast sequence perpendicular to direction of flow. Subsequent measurements were performed on 27 volunteers and 14 patients with stenosis. Our results showed flow decreases as stenosis degree increases where in 8 mm tubes, flow is stable up to 75 % stenosis while in 4 mm tubes; flow is stable up to 65 %. In healthy volunteers, flow difference between both sides ranges from 0.4-11% while for patients; flow difference was more than 15% depending on degree of stenosis. Patients had reduced flow in stenotic arteries compared to flow in normal volunteers. We concluded that QMRA is powerful tool in in assessment of stenosis affecting variable vessels. Proper sequence optimization is necessary for successful flow measurements. Flow behavior in response to stenosis varies among subjects compared to phantom measurements; this could be attributed be age, anatomy, physiological factors such as breathing in healthy subjects. While in patients, various pathological conditions would definitely affect blood flow such as underlying coronary disease, Hypertension. The continuation of this thesis would be to application of QMRA in patients with stents either in implanted in internal carotid artery and or in intracranial arteries. It might be applied in performing a flow profile for vessels before stenting and in follow up post-stenting on regular intervals in substitution of DSA and Doppler sonography; this would help tremendously in setting management plan optimized for every patient’s health condition.

Zusammenfassung

Schlaganfall stellt die dritthäufigste Todesursache und Hauptursache für Behinderung weltweit. Stenosen der A. carotis interna durch Atherosklerose sind für fast 30-40% der ischämischen Schlaganfälle verantwortlich Intrakranielle Stenosen sind für 20-40% der Schlaganfälle verantwortlich. Stenting wird zur Wiederherstellung der Gefäßdurchgängigkeit verwendet. In-Stent Restenosen treten in 25-35% der Patienten auf. MRT-Flussquantifizierung ist eine Alternative zur Diagnose von Stenosen durch ihre physiologische Wirkung. Einschränkungen ergeben sich durch Artefakte, welche durch das metallische Stentmaterial erzeugt werden. Ziel dieses Projektes war die Implementierung und Optimierung von MR-Sequenzen für die räumliche und zeitaufgelöste Flusskodierung sowie für die Abschätzung der Strömungsgeschwindigkeiten, um eine verbesserte Charakterisierung der Stenose und Bewertung ihres Grades zu erreichen. Ein selbstgebautes Phantom-Modell imitiert die normale Anatomie der Arteria carotis interna und der Arteria cerebri media: Rohre in Y-Form mit Durchmesser d = 8 und 4 mm, und eine pulsierende Pumpe (500 ml bei einer Rate von 60 Pulsen / min. Verschiedene Stenosegrade werden in einem Zweig erzeugt. Es wurde mit einer Phasenkontrast-Sequenz senkrecht zur Strömungsrichtung gemessen. Mit steigendem Stenosegrad nimmt der Fluss ab. In den 8-mm-Röhrchen war der Fluss bis 75% Stenose stabil, in den 4-mm-Röhrchen bis 65% Stenose. Nachfolgend wurden Messungen an 27 gesunden Probanden und 14 Patienten mit Carotis-Stenose durchgeführt. Bei gesunden Probanden liegt die Flussdifferenz zwischen der linken und der rechten Arterie im Bereich von 0,4 bis 11%, während für Patienten die Flussdifferenzen über 15% lagen, je nach Grad der Stenose. Patienten zeigten im Vergleich zu gesunden Probanden einen reduzierten Fluss in den stenotischen Arterien. Zusammenfassend kann festgestellt werden, dass die Quantitative Magnetresonanzangiographie ein nicht-invasives Tool für die Flussquantifizierung und Bewertung von Stenosen ist, welches auch bei bereits vorhandenen Stents angewandt werden kann. Die Ergebnisse können direkt für die Behandlungsplanung herangezogen werden.

8-Bibiliography

1. Taylor TN, Davis PH, Torner JC, Holmes J, Meyer JW, Jacobson MF. Lifetime cost of stroke in the United States. Stroke; a journal of cerebral circulation. 1996;27(9):1459-66.
2. Debrey SM, Yu H, Lynch JK, Lovblad KO, Wright VL, Janket SJ, et al. Diagnostic accuracy of magnetic resonance angiography for internal carotid artery disease: a systematic review and meta-analysis. Stroke; a journal of cerebral circulation. 2008;39(8):2237-48.
3. Korogi Y, Takahashi M, Nakagawa T, Mabuchi N, Watabe T, Shiokawa Y, et al. Intracranial vascular stenosis and occlusion: MR angiographic findings. AJNR American journal of neuroradiology. 1997;18(1):135-43.
4. Investigators SS. Stenting of Symptomatic Atherosclerotic Lesions in the Vertebral or Intracranial Arteries (SSYLVIA): study results. Stroke; a journal of cerebral circulation. 2004;35(6):1388-92.
5. Khan M NI, Kamal A K. Neuroimaging of intracranial atherosclerotic diseases. In: Bright P, editor. Neuroimaging-Clinical Applications InTech; 2012. p. 576.
6. Bash S, Villablanca JP, Jahan R, Duckwiler G, Tillis M, Kidwell C, et al. Intracranial vascular stenosis and occlusive disease: evaluation with CT angiography, MR angiography, and digital subtraction angiography. AJNR American journal of neuroradiology. 2005;26(5):1012-21.
7. Platzek I, Sieron D, Wiggermann P, Laniado M. Carotid Artery Stenosis: Comparison of 3D Time-of-Flight MR Angiography and Contrast-Enhanced MR Angiography at 3T. Radiology research and practice. 2014;2014:508715.
8. Meier D, Maier S, Bosiger P. Quantitative flow measurements on phantoms and on blood vessels with MR. Magnetic resonance in medicine. 1988;8(1):25-34.
9. Bucek RA, Puchner S, Haumer M, Rand T, Sabeti S, Minar E, et al. Grading of internal carotid artery stenosis: comparative analysis of different flow velocity criteria and multidetector computed tomographic angiography. Journal of endovascular therapy : an official journal of the International Society of Endovascular Specialists. 2006;13(2):182-9.
10. Zhao M, Charbel FT, Alperin N, Loth F, Clark ME. Improved phase-contrast flow quantification by three-dimensional vessel localization. Magnetic resonance imaging. 2000;18(6):697-706.
11. Jiang WJ, Xu XT, Jin M, Du B, Dong KH, Dai JP. Apollo stent for symptomatic atherosclerotic intracranial stenosis: study results. AJNR American journal of neuroradiology. 2007;28(5):830-4.
12. Levy EI, Turk AS, Albuquerque FC, Niemann DB, Aagaard-Kienitz B, Pride L, et al. Wingspan in-stent restenosis and thrombosis: incidence, clinical presentation, and management. Neurosurgery. 2007;61(3):644-50; discussion 50-1.
13. Maintz D, Grude M, Fallenberg EM, Heindel W, Fischbach R. Assessment of coronary arterial stents by multislice-CT angiography. Acta radiologica. 2003;44(6):597-603.
14. Orbach DB, Pramanik BK, Lee J, Maldonado TS, Riles T, Grossman RI. Carotid artery stent implantation: evaluation with multi-detector row CT angiography and virtual angioscopy--initial experience. Radiology. 2006;238(1):309-20.
15. Frolich AM, Pilgram-Pastor SM, Psychogios MN, Mohr A, Knauth M. Comparing different MR angiography strategies of carotid stents in a vascular flow model: toward stent-specific recommendations in MR follow-up. Neuroradiology. 2011;53(5):359-65.
16. Snell's Clinical Neuroanatomy 7ed. Philadelphia: Lippincott Williams Wilkins; 2010.
17. Murray CJ, Vos T, Lozano R, Naghavi M, Flaxman AD, Michaud C, et al. Disability-adjusted life years (DALYs) for 291 diseases and injuries in 21 regions, 1990-2010: a systematic analysis for the Global Burden of Disease Study 2010. Lancet. 2012;380(9859):2197-223.

18. Hankey GJ, Warlow CP. Treatment and secondary prevention of stroke: evidence, costs, and effects on individuals and populations. Lancet. 1999;354(9188):1457-63.
19. Kolominsky-Rabas PL, Heuschmann PU, Marschall D, Emmert M, Baltzer N, Neundorfer B, et al. Lifetime cost of ischemic stroke in Germany: results and national projections from a population-based stroke registry: the Erlangen Stroke Project. Stroke; a journal of cerebral circulation. 2006;37(5):1179-83.
20. Evers SM, Engel GL, Ament AJ. Cost of stroke in The Netherlands from a societal perspective. Stroke; a journal of cerebral circulation. 1997;28(7):1375-81.
21. Wong KS, Ng PW, Tang A, Liu R, Yeung V, Tomlinson B. Prevalence of asymptomatic intracranial atherosclerosis in high-risk patients. Neurology. 2007;68(23):2035-8.
22. Savitz SI, Caplan LR. Vertebrobasilar disease. The New England journal of medicine. 2005;352(25):2618-26.
23. Wong LK. Global burden of intracranial atherosclerosis. International journal of stroke : official journal of the International Stroke Society. 2006;1(3):158-9.
24. Sacco RL, Kargman DE, Gu Q, Zamanillo MC. Race-ethnicity and determinants of intracranial atherosclerotic cerebral infarction. The Northern Manhattan Stroke Study. Stroke; a journal of cerebral circulation. 1995;26(1):14-20.
25. Wityk RJ, Lehman D, Klag M, Coresh J, Ahn H, Litt B. Race and sex differences in the distribution of cerebral atherosclerosis. Stroke; a journal of cerebral circulation. 1996;27(11):1974-80.
26. Arenillas JF, Alvarez-Sabin J, Montaner J, Rosell A, Molina CA, Rovira A, et al. Angiogenesis in symptomatic intracranial atherosclerosis: predominance of the inhibitor endostatin is related to a greater extent and risk of recurrence. Stroke; a journal of cerebral circulation. 2005;36(1):92-7.
27. Sertic J, Hebrang D, Janus D, Salzer B, Niksic M, Cvoriscec D, et al. Association between deletion polymorphism of the angiotensin-converting enzyme gene and cerebral atherosclerosis. European journal of clinical chemistry and clinical biochemistry : journal of the Forum of European Clinical Chemistry Societies. 1996;34(4):301-4.
28. Uehara T, Tabuchi M, Hayashi T, Kurogane H, Yamadori A. Asymptomatic occlusive lesions of carotid and intracranial arteries in Japanese patients with ischemic heart disease: evaluation by brain magnetic resonance angiography. Stroke; a journal of cerebral circulation. 1996;27(3):393-7.
29. Rincon F, Sacco RL, Kranwinkel G, Xu Q, Paik MC, Boden-Albala B, et al. Incidence and risk factors of intracranial atherosclerotic stroke: the Northern Manhattan Stroke Study. Cerebrovascular diseases. 2009;28(1):65-71.
30. Arenillas JF, Molina CA, Chacon P, Rovira A, Montaner J, Coscojuela P, et al. High lipoprotein (a), diabetes, and the extent of symptomatic intracranial atherosclerosis. Neurology. 2004;63(1):27-32.
31. Tong E, Hou Q, Fiebach JB, Wintermark M. The role of imaging in acute ischemic stroke. Neurosurgical focus. 2014;36(1):E3.
32. Carvalho M, Oliveira A, Azevedo E, Bastos-Leite AJ. Intracranial arterial stenosis. Journal of stroke and cerebrovascular diseases : the official journal of National Stroke Association. 2014;23(4):599-609.
33. Klotzsch C, Popescu O, Sliwka U, Mull M, Noth J. Detection of stenoses in the anterior circulation using frequency-based transcranial color-coded sonography. Ultrasound in medicine & biology. 2000;26(4):579-84.
34. Wong KS, Gao S, Lam WW, Chan YL, Kay R. A pilot study of microembolic signals in patients with middle cerebral artery stenosis. Journal of neuroimaging : official journal of the American Society of Neuroimaging. 2001;11(2):137-40.

35. Oates CP, Naylor AR, Hartshorne T, Charles SM, Fail T, Humphries K, et al. Joint recommendations for reporting carotid ultrasound investigations in the United Kingdom. European journal of vascular and endovascular surgery : the official journal of the European Society for Vascular Surgery. 2009;37(3):251-61.
36. Nguyen-Huynh MN, Wintermark M, English J, Lam J, Vittinghoff E, Smith WS, et al. How accurate is CT angiography in evaluating intracranial atherosclerotic disease? Stroke; a journal of cerebral circulation. 2008;39(4):1184-8.
37. Villablanca JP, Rodriguez FJ, Stockman T, Dahliwal S, Omura M, Hazany S, et al. MDCT angiography for detection and quantification of small intracranial arteries: comparison with conventional catheter angiography. AJR American journal of roentgenology. 2007;188(2):593-602.
38. Feldmann E, Wilterdink JL, Kosinski A, Lynn M, Chimowitz MI, Sarafin J, et al. The Stroke Outcomes and Neuroimaging of Intracranial Atherosclerosis (SONIA) trial. Neurology. 2007;68(24):2099-106.
39. Rothwell PM, Gutnikov SA, Warlow CP, European Carotid Surgery Trialist's C. Reanalysis of the final results of the European Carotid Surgery Trial. Stroke; a journal of cerebral circulation. 2003;34(2):514-23.
40. Wada K, Kimura K, Minematsu K, Uchino M, Yamaguchi T. Spotty cortical enhancement detected by magnetic resonance imaging: a sign of embolic transient ischemic attack and stroke? Journal of stroke and cerebrovascular diseases : the official journal of National Stroke Association. 2001;10(1):19-22.
41. Yuan C, Murakami JW, Hayes CE, Tsuruda JS, Hatsukami TS, Wildy KS, et al. Phased-array magnetic resonance imaging of the carotid artery bifurcation: preliminary results in healthy volunteers and a patient with atherosclerotic disease. Journal of magnetic resonance imaging : JMRI. 1995;5(5):561-5.
42. Yuan C, Kerwin WS, Yarnykh VL, Cai J, Saam T, Chu B, et al. MRI of atherosclerosis in clinical trials. NMR in biomedicine. 2006;19(6):636-54.
43. Ma N, Lou X, Zhao TQ, Wong EH, Jiang WJ. Intraobserver and interobserver variability for measuring the wall area of the basilar artery at the level of the trigeminal ganglion on high-resolution MR images. AJNR American journal of neuroradiology. 2011;32(2):E29-32.
44. Zhao M, Amin-Hanjani S, Ruland S, Curcio AP, Ostergren L, Charbel FT. Regional cerebral blood flow using quantitative MR angiography. AJNR American journal of neuroradiology. 2007;28(8):1470-3.
45. Brisman JL, Pile-Spellman J, Konstas AA. Clinical utility of quantitative magnetic resonance angiography in the assessment of the underlying pathophysiology in a variety of cerebrovascular disorders. European journal of radiology. 2012;81(2):298-302.
46. Amin-Hanjani S, Du X, Zhao M, Walsh K, Malisch TW, Charbel FT. Use of quantitative magnetic resonance angiography to stratify stroke risk in symptomatic vertebrobasilar disease. Stroke; a journal of cerebral circulation. 2005;36(6):1140-5.
47. Bauer AM, Amin-Hanjani S, Alaraj A, Charbel FT. Quantitative magnetic resonance angiography in the evaluation of the subclavian steal syndrome: report of 5 patients. Journal of neuroimaging : official journal of the American Society of Neuroimaging. 2009;19(3):250-2.
48. Brisman JL. Wingspan stenting of symptomatic extracranial vertebral artery stenosis and perioperative evaluation using quantitative magnetic resonance angiography: report of two cases. Neurosurgical focus. 2008;24(2):E14.
49. Ruland S, Ahmed A, Thomas K, Zhao M, Amin-Hanjani S, Du X, et al. Leptomeningeal collateral volume flow assessed by quantitative magnetic resonance angiography in large-vessel cerebrovascular disease. Journal of neuroimaging : official journal of the American Society of Neuroimaging. 2009;19(1):27-30.

50. Langer DJ, Song JK, Niimi Y, Chwajol M, Lefton DR, Brisman JL, et al. Transarterial embolization of vein of Galen malformations: the use of magnetic resonance imaging noninvasive optimal vessel analysis to quantify shunt reduction. Report of two cases. Journal of neurosurgery. 2006;104(1 Suppl):41-5.
51. Kellner-Weldon F. Quantitative magnetic resonance angiography. Clinical neuroradiology. 2012;22(1):115-8.
52. Nasimi A. Hemodynamics. In: Gaze D, editor. The Cardiovascular system-Physioloiogy,Diagnostics and Clinical Implications: InTech; 2012. p. 478.
53. Shanthoshini Deviha V, P. R, R. JH. Modeling Blood Flow in the Blood Vessels of the Cardiovascular System Using Fractals. Applied Mathematical Sciences. 2013;7(11):527-37.
54. Fung YC. Biomechanics - Motion, flow, stress and growth. New York,USA: Springer-Verlag; 1990.
55. Nicolaas W, Stergiopulos N, Noble MIM. Snapshots of Hemodynamics,An Aid for Clinical Research and Graduate Education. New York Springer; 2010.
56. Burton AC. Physiology and biophysics of the circulation. Chicago Year Book Medical Publishers; 1972.
57. Downing JM, Ku DN. Effects of frictional losses and pulsatile flow on the collapse of stenotic arteries. Journal of biomechanical engineering. 1997;119(3):317-24.
58. Ku DN, Zeigler MN, Downing JM. One-dimensional steady inviscid flow through a stenotic collapsible tube. Journal of biomechanical engineering. 1990;112(4):444-50.
59. M R, S E. The effect of constriction size on the pulsatile flow in a channel. ASME J Fluids Eng. 1995;117(4):571–76.
60. Seeley BD, Young DF. Effect of geometry on pressure losses across models of arterial stenoses. Journal of biomechanics. 1976;9(7):439-48.
61. Berger SA, Jou. L-D. Flows in stenotic vessels. Annual Review of Fluid Mechanics. 2000;32:347-82.
62. Bluestein D, Einav S. The effect of varying degrees of stenosis on the characteristics of turbulent pulsatile flow through heart valves. Journal of biomechanics. 1995;28(8):915-24.
63. Johnston PR, Kilpatrick D. Mathematical modelling of flow through an irregular arterial stenosis. Journal of biomechanics. 1991;24(11):1069-77.
64. Guyton AC, Hall JE. Text book of Medical Physiology. 11th ed. Philadelphia: Saunders/Elsevier; 2006. 1152 p.
65. Westbrook C, Roth CK, Talbot J. MRI in practice 4th ed. West Sussex: Wiley Blackwell; 2011. 459 p.
66. Markl M. Velocity encoding and flow imaging 2005 [12/08/2015]; Available from: http://ee-classes.usc.edu/ee591/library/Markl-FlowImaging.pdf.
67. Lee V.S. Cardiovascular MRI:physical principles to practical protocols Philadelphia Lippincott Williams and Wilkins; 2006.
68. Kumar GA, Chowdhury V, Khandelwal N. Diagnostic Radiology: Recent Advances and Applied Physics in Imaging 2nd ed: Jaypee Brothers Medical Pub; 2013.
69. Bernstein MA, King KF, Zhou X. Handbook of MRI pulse sequences Academic Press; 2004.
70. Lotz J, Doker R, Noeske R, Schuttert M, Felix R, Galanski M, et al. In vitro validation of phase-contrast flow measurements at 3 T in comparison to 1.5 T: precision, accuracy, and signal-to-noise ratios. Journal of magnetic resonance imaging : JMRI. 2005;21(5):604-10.
71. Bernstein Matt A, Kevin F. King, Zhou XJ. Basics of physiologic gating ,triggering and monitoring Handbook of MRI Pulse Sequences Elsevier Inc.; 2004. p. 1040.
72. http://www.healthcare.siemens.com/magnetic-resonance-imaging/3t-mri-scanner/magnetom-skyra/technical-details. 2015 [cited 2015 09/2015].

73. Hackbart A. Untersuchungen zur Quantifizierbarkeit von Fluss in gefäßähnlichen Phantomen Mittels MRT [Studienarbeit]: Stuttgart University; 2015.
74. Ota H, Takase K, Rikimaru H, Tsuboi M, Yamada T, Sato A, et al. Quantitative vascular measurements in arterial occlusive disease. Radiographics : a review publication of the Radiological Society of North America, Inc. 2005;25(5):1141-58.
75. Choi JW, Roh HG, Moon WJ, Chun YI, Kang CH. Optimization of MR Parameters of 3D TOF-MRA for Various Intracranial Stents at 3.0T MRI. Neurointervention. 2011;6(2):71-7.
76. Offerman EJ, Hodnett PA, Edelman RR, Koktzoglou I. Nonenhanced methods for lower-extremity MRA: a phantom study examining the effects of stenosis and pathologic flow waveforms at 1.5T. Journal of magnetic resonance imaging : JMRI. 2011;33(2):401-8.
77. Brandts A, Roes SD, Doornbos J, Weiss RG, de Roos A, Stuber M, et al. Right coronary artery flow velocity and volume assessment with spiral K-space sampled breathhold velocity-encoded MRI at 3 tesla: accuracy and reproducibility. Journal of magnetic resonance imaging : JMRI. 2010;31(5):1215-23.
78. Dambreville S, Chapman AB, Torres VE, King BF, Wallin AK, Frakes DH, et al. Renal arterial blood flow measurement by breath-held MRI: Accuracy in phantom scans and reproducibility in healthy subjects. Magnetic resonance in medicine. 2010;63(4):940-50.
79. Ho SS, Chan YL, Yeung DK, Metreweli C. Blood flow volume quantification of cerebral ischemia: comparison of three noninvasive imaging techniques of carotid and vertebral arteries. AJR American journal of roentgenology. 2002;178(3):551-6.
80. Hollnagel DI, Summers PE, Kollias SS, Poulikakos D. Laser Doppler velocimetry (LDV) and 3D phase-contrast magnetic resonance angiography (PC-MRA) velocity measurements: validation in an anatomically accurate cerebral artery aneurysm model with steady flow. Journal of magnetic resonance imaging : JMRI. 2007;26(6):1493-505.
81. Hoppe M, Heverhagen JT, Froelich JJ, Kunisch-Hoppe M, Klose KJ, Wagner HJ. Correlation of flow velocity measurements by magnetic resonance phase contrast imaging and intravascular Doppler ultrasound. Investigative radiology. 1998;33(8):427-32.
82. Ponzini R, Vergara C, Rizzo G, Veneziani A, Roghi A, Vanzulli A, et al. Womersley number-based estimates of blood flow rate in Doppler analysis: in vivo validation by means of phase-contrast MRI. IEEE transactions on bio-medical engineering. 2010;57(7):1807-15.
83. Stahlberg F, Sondergaard L, Thomsen C, Henriksen O. Quantification of complex flow using MR phase imaging--a study of parameters influencing the phase/velocity relation. Magnetic resonance imaging. 1992;10(1):13-23.
84. O'Brien KR, Cowan BR, Jain M, Stewart RA, Kerr AJ, Young AA. MRI phase contrast velocity and flow errors in turbulent stenotic jets. Journal of magnetic resonance imaging : JMRI. 2008;28(1):210-8.
85. Schubert T, Bieri O, Pansini M, Stippich C, Santini F. Peak velocity measurements in tortuous arteries with phase contrast magnetic resonance imaging: the effect of multidirectional velocity encoding. Investigative radiology. 2014;49(4):189-94.
86. Amin-Hanjani S, Du X, Pandey DK, Thulborn KR, Charbel FT. Effect of age and vascular anatomy on blood flow in major cerebral vessels. Journal of cerebral blood flow and metabolism : official journal of the International Society of Cerebral Blood Flow and Metabolism. 2015;35(2):312-8.
87. Matteis M, Caltagirone C, Troisi E, Vernieri F, Monaldo BC, Silvestrini M. Changes in cerebral blood flow induced by passive and active elbow and hand movements. Journal of neurology. 2001;248(2):104-8.
88. Shakur SF, Hrbac T, Alaraj A, Du X, Aletich VA, Charbel FT, et al. Effects of extracranial carotid stenosis on intracranial blood flow. Stroke; a journal of cerebral circulation. 2014;45(11):3427-9.

Erklärung zum Eigenanteil

Ahmed Sobieh shared in the design of the study, conducted phantom and some subject measurements, reviewed literature, analyzed data and wrote the manuscript.

Prof. Uwe Klose came up with the idea of this project and he put the design of this study, he supervised each step in the research thoroughly and corrected the manuscript.

Dr.Till Karsten Hauser shared in the design of this study and he recruited volunteers and patients for this study. He corrected the manuscript.

Arthur Hackbart constructed the 3rd phantom and builds its connection; He participated on experiments conducted on the 3rd phantom.

Tübingen den 19 October 2015

Ahmed Sobieh